

Radiative-transfer models for supernovae IIb/Ib/Ic from binary-star progenitors

Luc Dessart,^{1*} D. John Hillier,² Stan Woosley,³ Eli Livne,⁴ Roni Waldman,⁴
Sung-Chul Yoon,⁵ and Norbert Langer.⁶

¹: *Laboratoire Lagrange, Université Côte d’Azur, Observatoire de la Côte d’Azur, CNRS, Boulevard de l’Observatoire, CS 34229, 06304 Nice cedex 4, France.*

²: *Department of Physics and Astronomy & Pittsburgh Particle Physics, Astrophysics, and Cosmology Center (PITT PACC), University of Pittsburgh, 3941 O’Hara Street, Pittsburgh, PA 15260, USA.*

³: *Department of Astronomy and Astrophysics, University of California, Santa Cruz, CA 95064, USA.*

⁴: *Racah Institute of Physics, The Hebrew University, Jerusalem 91904, Israel.*

⁵: *Department of Physics and Astronomy, Seoul National University, Gwanak-ro 1, Gwanak-gu, Seoul, 151-742, Republic of Korea*

⁶: *Argelander-Institut für Astronomie, Universität Bonn, Auf dem Hügel 71, 53121, Bonn, Germany*

Accepted 2015 July 28. Received 2015 July 27; in original form 2015 June 11.

ABSTRACT

We present 1-D non-Local-Thermodynamic-Equilibrium time-dependent radiative-transfer simulations for supernovae (SNe) of type IIb, Ib, and Ic that result from the terminal explosion of the mass donor in a close-binary system. Here, we select three ejecta with a total kinetic energy of $\approx 1.2 \times 10^{51}$ erg, but characterised by different ejecta masses ($2\text{--}5 M_{\odot}$), composition, and chemical mixing. The type IIb/Ib models correspond to the progenitors that have retained their He-rich shell at the time of explosion. The type Ic model arises from a progenitor that has lost its helium shell, but retains $0.32 M_{\odot}$ of helium in a CO-rich core of $5.11 M_{\odot}$. We discuss their photometric and spectroscopic properties during the first 2–3 months after explosion, and connect these to their progenitor and ejecta properties including chemical stratification. For these three models, Arnett’s rule overestimates the ^{56}Ni mass by $\approx 50\%$ while the procedure of Katz et al., based on an energy argument, yields a more reliable estimate. The presence of strong C I lines around 9000\AA prior to maximum is an indicator that the pre-SN star was under-abundant in helium. As noted by others, the $1.08\mu\text{m}$ feature is a complex blend of C I, Mg II, and He I lines, which makes the identification of He uncertain in SNe Ibc unless other He I lines can be identified. Our models show little scatter in $(V - R)$ colour 10 d after R -band maximum. We also address a number of radiative transfer properties of SNe Ibc, including the notion of a photosphere, the inference of a representative ejecta expansion rate, spectrum formation, blackbody fits and “correction factors”.

Key words: radiation hydrodynamics – radiative transfer – stars: supernovae – stars: evolution – stars: binaries

1 INTRODUCTION

SNe IIb/Ib/Ic are understood to arise from the collapse of the iron core of massive stars having lost most (type IIb) or all (types Ib and Ic) of their envelope exterior to the He core. Wolf-Rayet stars are therefore the natural progenitors of these transient phenomena. However in the 80’s, after the first well sampled light curves of type I core-collapse SNe were obtained, it became evident that their ejecta were of low mass (Ensmann & Woosley 1988; Woosley et al. 1995), in accord with the binary evolution scenario

and moderate progenitor masses (Wellstein & Langer 1999). As wind mass loss rates for Wolf-Rayet stars were revised downwards (see, e.g., Hillier 1991, Nugis & Lamers 2000) and inferences for low SN Ib/c ejecta strengthened (Woosley et al. 1994; Dessart et al. 2011; Drout et al. 2011; Bersten et al. 2012; Hachinger et al. 2012; Benvenuto et al. 2013; Ergon et al. 2014; Jerkstrand et al. 2015), the binary star evolution channel became the main scenario for the production of type I core-collapse SNe (see, e.g., Yoon 2015).

An extensive study of binary evolution, and its implications for SN types, was made by Podsiadlowski et al. (1992). As part of their study, they estimated probabilities for various evolutionary scenarios for massive stars with masses between 8 and $20 M_{\odot}$.

* email: Luc.Dessart@oca.eu

Table 1. Summary of progenitor properties at the time of core collapse. The last column gives the iron-core mass.

Model	M_i [M_\odot]	M_f [M_\odot]	L_\star [erg s^{-1}]	T_{eff} [K]	R_\star [cm]	M_{CO} [M_\odot]	M_{Fe} [M_\odot]
3p65	16.0	3.65	2.16(38)	21 700	1.17(12)	2.03	1.43
5p11	60.0	5.11	5.42(38)	130 000	5.19(10)	3.64	1.52
6p5	25.0	6.50	6.40(38)	68 700	2.01(11)	4.21	1.48

They concluded that a complete understanding of massive star evolution will only be obtained when we understand binary star evolution. This also requires a census of binaries and their parameters. A more recent study is that of Claeys et al. (2011) who studied the roles of binaries in producing type IIb SNe.

In this first paper of a series we perform 1-D non-Local-Thermodynamic-Equilibrium (non-LTE) time-dependent radiative-transfer simulations for supernovae of type IIb, Ib, and Ic that result from the terminal explosion of the primary star in a close-binary system. The progenitor models are taken from the study of Yoon et al. (2010), which treats the evolution from the main sequence until neon burning. The later stages of evolution, and the subsequent explosion is done with KEPLER (Woosley et al., in preparation; Weaver et al. 1978; Section 2).

This endeavour extends beyond the previous studies of Dessart et al. (2011, 2012) by using better physics, a broader range of progenitors, and a broader range of explosion energies and ^{56}Ni mass. In Dessart et al. (2011), non-thermal effects and chemical mixing were ignored. In Dessart et al. (2012), the focus was on mixing alone, based on only two explosion models with the same energy. Both progenitor models had a large helium mass. Here, the full set comprises about 30 model sequences covering a much broader parameter space. We compute full time sequences in non-LTE, with allowance for time dependence, non-thermal effects and non-local energy deposition (Section 2). Throughout this series, we limit the discussion to the photospheric phase. The nebular phase properties, because they are so strongly connected to the nature of mixing, will be treated in a separate study. Our goal is to characterise the light curve and spectral properties of SNe IIb/Ib/Ic and correlate them to the explosion model and to the progenitor star. This includes a discussion of the bolometric light curves, multi-band light curves, colour evolution (Section 3), spectral evolution (Section 4), the properties of near-IR He I lines (Section 5), the influence of mixing (Section 6), the properties of spectrum formation and the notion of a photosphere in type I SNe (Section 7), the inference of the ejecta expansion rate and the constraint on chemical stratification (Section 8), and the correction factors to be used when approximating the synthetic spectra of SNe IIb/Ib/Ic near maximum light with a blackbody (Section 9).

In Section 10, we summarise the results of the present paper. In Paper II, we will do a statistical study based on the entire grid of about 30 model sequences to examine correlations/distinction between the models. In Paper III, we will use our grid of models to compare to observations of SNe IIb/Ib/Ic.

2 NUMERICAL SETUP AND INITIAL CONDITIONS

2.1 Pre-supernova evolution, explosion, and supernova radiative transfer

Yoon et al. (2010) computed the evolution from the main sequence

Table 2. Summary of ejecta properties. The last three columns give the ejecta velocity that bounds 99% of the corresponding species total mass. The integration is done inwards in velocity space for H and He, and outwards for ^{56}Ni .

Model	M_r [M_\odot]	M_e [M_\odot]	E_{kin} [B]	$V_{99,\text{H}}$ [km s^{-1}]	$V_{99,\text{He}}$ [km s^{-1}]	$V_{99,\text{Ni}}$ [km s^{-1}]
3p65Ax1	1.43	2.22	1.24	1.34(4)	3.06(3)	7.00(3)
3p65Ax2	1.43	2.22	1.22	1.24(4)	2.62(3)	1.01(4)
5p11Ax1	1.57	3.54	1.25	...	1.68(3)	6.20(3)
5p11Ax2	1.52	3.59	1.29	...	2.71(3)	9.18(3)
6p5Ax1	1.53	4.97	1.26	...	3.28(3)	5.98(3)
6p5Ax2	1.55	4.95	1.25	...	2.55(3)	8.60(3)

until the end of neon burning, including differential rotation, tides and mass and angular momentum transfer, for a limited set of close-binary systems (orbital period of ≈ 4 d), covering a range of primary-star masses (12 to $60 M_\odot$) and mass ratios ($\gtrsim 1-1.5$). These simulations were then evolved to core collapse (Woosley et al., in preparation), and subsequently exploded with KEPLER using a piston.

We have performed a grid of explosion models, corresponding to the binary models in the Yoon et al. study that are numbered Yoon_13 (the final mass of the primary star, $M_{1,f}$, is $3.0 M_\odot$), Yoon_9 ($M_{1,f} = 3.65 M_\odot$), Yoon_35 ($M_{1,f} = 4.64 M_\odot$; $Z = 0.004$), Yoon_31¹ ($M_{1,f} = 5.11 M_\odot$), and Yoon_30 ($M_{1,f} = 6.5 M_\odot$). All models use the solar composition initially, except model Yoon_35. This choice includes models with residual surface hydrogen (Yoon_13, 9, 35), no hydrogen but high helium and nitrogen abundances (Yoon_30), and little helium but high abundance of carbon and oxygen (Yoon_31).

In this paper, we limit the discussion to just three progenitor models, 3p65, 5p11, and 6p5 (Table 1). Their diversity in envelope composition leads them to produce, after explosion, the three common type I core-collapse SN IIb, Ib, and Ic. Models 3p0 and 4p64 will be discussed in Papers II and III.

Upon reaching core collapse, each model was exploded with KEPLER to produce ejecta with an asymptotic kinetic energy of 0.6 (suffix C), 1.2 (suffix A), 2.4 (suffix B), and 5×10^{51} erg (suffix D). In practice, the lower mass models were limited to lower energy explosions ($0.6-2.4 \times 10^{51}$ erg). Explosive nucleosynthesis is treated in KEPLER and therefore these simulations naturally produce some ^{56}Ni . Higher energy explosions exhibit higher post-shock temperatures, which favour ^{56}Ni production. The full set of explosion models is characterised by an original ^{56}Ni mass of $0.05-0.2 M_\odot$. Here, we only discuss ‘‘A’’ models, characterised by a kinetic energy at infinity of $\approx 1.2 \times 10^{51}$ erg.

These explosion models were then remapped into $\check{\text{I}}\text{d}$ (Livne 1993; Dessart et al. 2010a,b) at 10^4 s and evolved to 10^5 s. This additional step is to explore a different mixing approach from that employed in KEPLER. In our 1-D approach, we take the multi-dimensional process of mixing (Fryxell et al. 1991; Kifonidis et al. 2006; Hammer et al. 2010; Wongwathanarat et al. 2014) into account by applying a simple algorithm. Starting from the ejecta

¹ This model has a final mass of $5.11 M_\odot$, and not $4.96 M_\odot$ as given in Table 1 of Yoon et al. (2010). This is because the remapping of this model into KEPLER was done at an earlier stage and the final evolution to core collapse neglected wind mass loss.

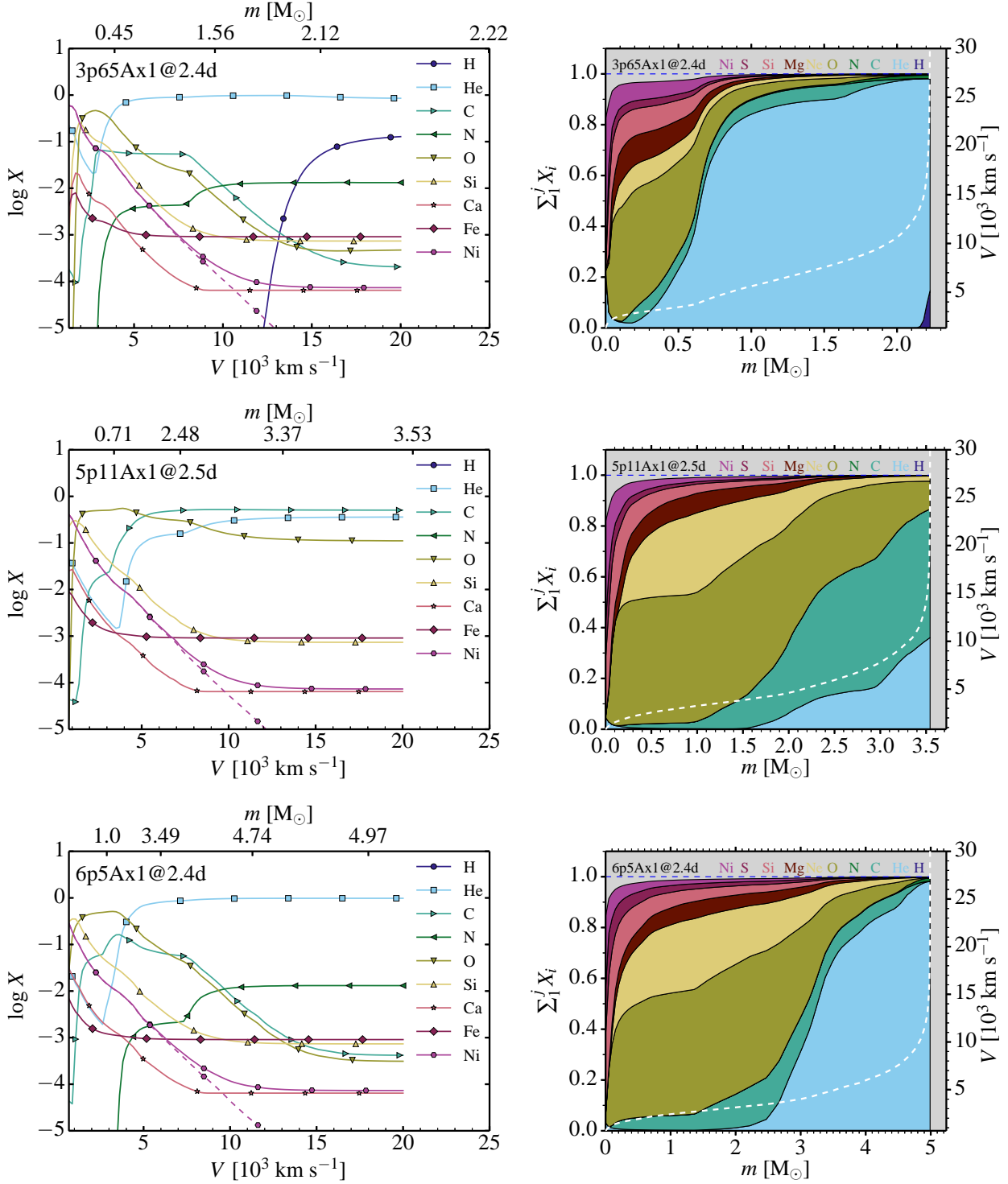


Figure 1. Ejecta composition at ≈ 2.5 d after explosion for models 3p65Ax1 (top row), 5p11Ax1 (middle row), and 6p5Ax1 (bottom row). In the left column, we show the mass fraction versus velocity for a selection of species. The dashed line corresponds to ^{56}Ni . The top axis gives the lagrangian mass coordinate. For clarity, the curve for ^{56}Co is not shown; at 2.5 d it amounts to $\approx 1/4$ of the ^{56}Ni mass. In the right column, we show for each mass shell m the cumulative mass fraction $\sum_1^j X_i(m)$, where i covers species H, He, C, N, O, Ne, Mg, Si, S, and Ni (for Ni, we show the current total mass fraction, which therefore accounts for decays). We also show the velocity (dashed line, right axis). This illustration reveals more clearly the relative fraction occupied by abundant species. The variable size of the mass buffer between the He-rich layers and the ^{56}Ni rich layers is key to understand the production of He I lines.

Table 3. Cumulative yields for our grid of models at ≈ 2 d after explosion. For ^{56}Ni , we give the original mass, i.e., prior to decay. Models with different mixing show slightly different levels of fallback, and consequently show slightly different yields.

Model	H [M_{\odot}]	He [M_{\odot}]	C [M_{\odot}]	N [M_{\odot}]	O [M_{\odot}]	Si [M_{\odot}]	S [M_{\odot}]	Ca [M_{\odot}]	$(^{56}\text{Ni})_0$ [M_{\odot}]
3p65Ax1	4.99(-3)	1.49(0)	9.40(-2)	1.09(-2)	3.02(-1)	7.38(-2)	2.36(-2)	3.94(-3)	7.42(-2)
3p65Ax2	4.72(-3)	1.48(0)	9.37(-2)	1.08(-2)	3.01(-1)	7.30(-2)	2.33(-2)	3.91(-3)	7.66(-2)
5p11Ax1	0	3.15(-1)	8.92(-1)	0	1.42(0)	1.28(-1)	4.00(-2)	5.98(-3)	8.94(-2)
5p11Ax2	0	3.26(-1)	9.23(-1)	0	1.44(0)	1.28(-1)	4.04(-2)	6.13(-3)	9.46(-2)
6p5Ax1	0	1.67(0)	4.13(-1)	7.59(-3)	1.57(0)	2.12(-1)	9.31(-2)	9.30(-3)	9.90(-2)
6p5Ax2	0	1.66(0)	4.11(-1)	7.52(-3)	1.57(0)	2.14(-1)	9.40(-2)	9.51(-3)	1.02(-1)

Table 4. Mass fractions for some important species in the outermost mass shell for our grid of models. This shell corresponds to the progenitor surface. The same outermost-shell composition is obtained for the x2-model counterparts (hence not shown).

Model	$X_{\text{H},s}$	$X_{\text{He},s}$	$X_{\text{C},s}$	$X_{\text{N},s}$	$X_{\text{O},s}$	$X_{\text{Si},s}$	$X_{\text{S},s}$	$X_{\text{Ca},s}$	$X_{\text{Fe},s}$
3p65Ax1	1.480(-1)	8.332(-1)	1.980(-4)	1.320(-2)	4.831(-4)	7.352(-4)	3.651(-4)	6.442(-5)	9.086(-4)
5p11Ax1	0	3.611(-1)	5.051(-1)	0	1.100(-1)	7.362(-4)	3.651(-4)	6.442(-5)	9.097(-4)
6p5Ax1	0	9.813(-1)	4.147(-4)	1.309(-2)	3.098(-4)	7.345(-4)	3.647(-4)	6.435(-5)	9.086(-4)

base, we make homogeneous all mass shells within 1000 (x1) or 2000 km s^{-1} (x2), and sweep this mixing-box through all mass shells all the way to the outermost ejecta layers.² This mixing box is thus applied hundreds of times (i.e., the number of times is equal to the number of grid points in the model). Because of the overwhelming evidence that SN Ib/c ejecta are mixed (Lucy 1991; Dessart et al. 2012), we do not include unmixed models. But because the magnitude of mixing is very uncertain, we use two values corresponding to moderate and strong mixing. Our approach enforces a macroscopic mixing (large scale mixing of species over a wide range of velocities) as well as a microscopic mixing (each mass shell is homogeneous with no segregation of species at a given velocity). Multi-dimensional simulations of core-collapse SNe predict strong macroscopic mixing, but very limited microscopic mixing (e.g., Wongwathanarat et al. 2014, and references there in). Observationally, this distinction becomes evident at nebular times (Jerkstrand et al. 2015). Models with different mixing produce ejecta that suffer a slightly different fallback. This leads to small variations in yields (Table 3).

Our nomenclature is to name each model according to its final mass. For example, model 3p65Ax1 corresponds to model Yoon₉ which died as a $3.65 M_{\odot}$ star. It was exploded to yield an asymptotic kinetic energy of 1.2×10^{51} erg, and was mixed with a velocity width of 1000 km s^{-1} .

At 10^5 s, all models are remapped onto the grid of the non-LTE radiative transfer code CMFGEN and evolved until nebular times (Hillier & Dessart 2012). The entire ejecta is treated, and each model is evolved with the same physics. We treat non-thermal processes (Dessart et al. 2012; Li et al. 2012) and time dependence (Dessart & Hillier 2008). The γ -ray energy deposition is computed using a Monte Carlo approach (Hillier & Dessart 2012), and for this study only the decay of ^{56}Ni is taken into account. We en-

² In KEPLER, the width of the mixing box is specified in mass space rather than velocity space. This is problematic for species like H and He that may be present only in the outermost layers of the progenitor star, potentially introducing some mixing out to the largest velocities in low mass ejecta, which is probably unphysical.

force a minimum mass fraction for metals not included in the small network of 19 isotopes used in the pre-SN simulations, and assign them their solar metallicity value. The model atoms are the same as those used in Dessart et al. (2013a), with the updates for forbidden line transitions discussed in Dessart et al. (2014).

Convolving the emergent flux computed with CMF_FLUX (Busche & Hillier 2005) over filter bandpasses and integrating over the full frequency range, we directly extract the photometric and bolometric properties of all model sequences. Because of the different physics treated in `ld` and CMFGEN, a few time steps are needed to relax the ejecta initially, in particular in the regions with a Roseland mean optical depth less than a few. Hence, we only show the results for expansion ages greater than ≈ 2 d.

The main deficiencies of the present simulations are the limitation to close-binary progenitors and the use of a mixing procedure that is simplistic. We are in the process of curing these deficiencies.

2.2 Summary of ejecta properties

Although model ejecta masses are lower than $\approx 5 M_{\odot}$, there is great disparity in the ejecta composition. Model 3p65 has some residual hydrogen in its outermost layers, with a total mass of $0.005 M_{\odot}$ and a maximum mass fraction of 0.14. It constitutes a prototype for a type IIb event (Dessart et al. 2011).

Models 3p65 and 6p5 have a massive He-rich shell of about $1 M_{\odot}$ in which the helium mass fraction is $\gtrsim 90\%$. This shell represents a large fraction of the total ejecta mass, from $\approx 70\%$ in model 3p65 down to 35% in model 6p5. As we discuss in Dessart et al. (2012), the larger that fraction the greater the likelihood of exciting He I lines and producing a SN Ib (or IIb if hydrogen is present). Model 5p11 is hydrogen deficient and exhibits a balanced mixture of He, C, and O at its surface.

If all these progenitors were luminous enough to drive an optically-thick wind and produce an emission-line spectrum, models 3p65 and 6p5 would correspond to a WN or WNH type, but model 5p11 would clearly be of WC type. Model 5p11 has lost its He-rich shell (that shell made of $\gtrsim 90\%$ helium). Its surface is

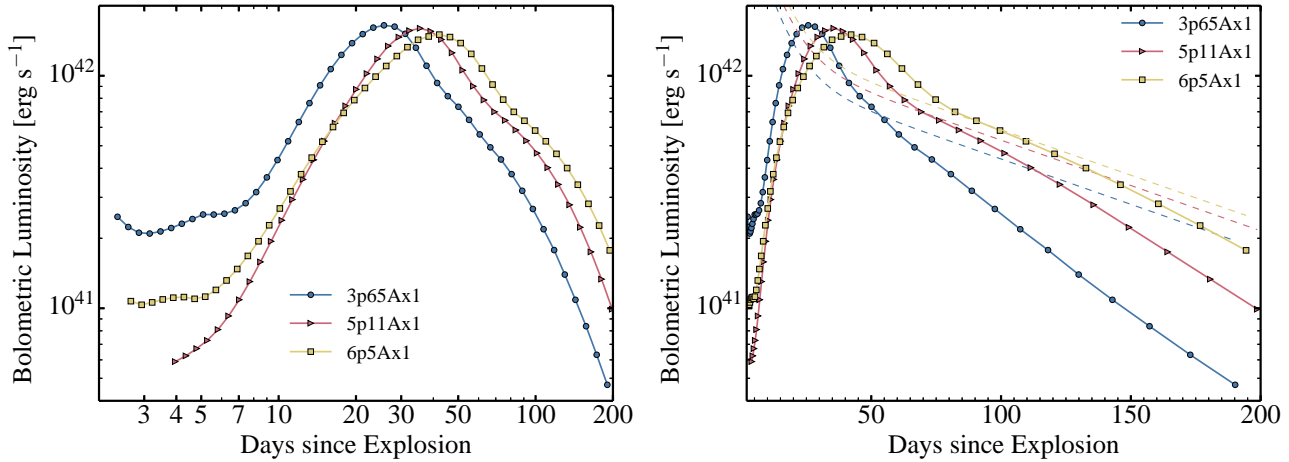


Figure 2. Bolometric luminosity light curve for models 3p65Ax1, 5p11Ax1, and 6p5Ax1. We use a logarithmic scale for the x -axis in the left panel to show the contrast in early-time luminosity and the possible existence of a short-lived post-breakout plateau (even in the presence of mixing). The right panel shows the full evolution, and in particular the increase in the peak delay, light curve width, and nebular brightness for higher mass ejecta (associated in this context with the higher γ -ray trapping efficiency). For each model, we overlay the decay power associated with ^{56}Ni and its daughter isotope ^{56}Co (dashed line).

Table 5. Luminosity and photometric properties for our model set. For each entry, we give the rise time to maximum, the value at peak, and the corresponding magnitude change between the time of peak and 15 d later. The R-band maximum occurs within 1 day of the bolometric maximum.

[mag] Model	L_{bol}			$L_{\text{UV+OIR}}$			U			B		
	t_{rise} [d]	Max. [erg s^{-1}]	ΔM_{15} [mag]	t_{rise} [d]	Max. [erg s^{-1}]	ΔM_{15} [mag]	t_{rise} [d]	Max. [mag]	ΔM_{15} [mag]	t_{rise} [d]	Max. [mag]	ΔM_{15} [mag]
3p65Ax1	2.631(1)	1.648(42)	6.157(-1)	2.579(1)	1.290(42)	6.956(-1)	2.387(1)	-1.576(1)	1.157(0)	2.410(1)	-1.662(1)	1.028(0)
5p11Ax1	3.584(1)	1.590(42)	3.939(-1)	3.506(1)	1.182(42)	4.234(-1)	3.208(1)	-1.524(1)	6.838(-1)	3.256(1)	-1.633(1)	5.941(-1)
6p5Ax1	4.212(1)	1.495(42)	2.262(-1)	4.057(1)	1.079(42)	2.449(-1)	3.634(1)	-1.497(1)	2.554(-1)	3.668(1)	-1.606(1)	3.623(-1)

within the C-rich part of the CO core. This model appears more suitable to produce a type Ic SN.

In this paper we focus on three models, endowed with the same ejecta kinetic energy at infinity of $\approx 1.2 \times 10^{51}$ erg, but different masses and composition. These models, in order of increasing pre-SN mass, are 3p65Ax1, 5p11Ax1, and 6p5Ax1. The models have initial ^{56}Ni masses of 0.074 to 0.099 M_{\odot} . This is somewhat smaller than the mean of 0.2 M_{\odot} inferred by Drout et al. (2011) for SNe Ibc, but there is considerable scatter within the class. Progenitor and ejecta properties are summarised in Tables 2–4, while the composition for each SN model is shown in velocity and Lagrangian-mass spaces in Fig. 1.

The goal with this restricted set is to discuss the salient features of type IIb, Ib, and Ic rather than correlate the properties of their light curves and spectra with those of the progenitor and explosion — this will be done in Paper II. We also address the influence of mixing by comparing these models to the “x2” counterpart, i.e., 3p65Ax2, 5p11Ax2, 6p5Ax2 (Section 6). The description of the full model set is deferred to Paper II.

3 PHOTOMETRIC EVOLUTION

3.1 Bolometric light curve

After shock emergence, the light curve of a SN is controlled by the simultaneous effects of cooling, heating, and energy transport.³ The cooling is initially primarily caused by expansion until the ejecta reaches a large radius. When the ejecta turn optically thin, cooling is primarily by radiation. The dominant heating source is radioactive decay, with a small contribution from recombination at early times.

The shocked envelope holds a large internal energy at shock breakout (about 50% of the total ejecta energy at that time). Despite the degradation by expansion of this shock-deposited energy, the SN is still significantly luminous a few days after the explosion. A post-breakout plateau of the order of 10^{41} erg s^{-1} is seen in the larger mass model 6p5Ax1, while mixing in the lower mass models leads to a gradual brightening by 2–3 days (Fig. 2).

This post-breakout luminosity is function of the progenitor radius, ejecta mass, and the amount and spatial distribution of ^{56}Ni (Woosley et al. 1994; Dessart et al. 2011; Bersten et al. 2012; Piro & Nakar 2013; Nakar & Piro 2014). In this work, all progen-

³ By definition, the bolometric luminosity includes contributions at all wavelengths. However, here we adopt the usual convention in SN modeling, and exclude the contribution of gamma-rays which generally cannot be measured.

Table 6. Same as Table 5, but now for the V , R , and I bands.

Model	V			R			I		
	t_{rise} [d]	Max. [mag]	ΔM_{15} [mag]	t_{rise} [d]	Max. [mag]	ΔM_{15} [mag]	t_{rise} [d]	Max. [mag]	ΔM_{15} [mag]
3p65Ax1	2.551(1)	-1.723(1)	7.828(-1)	2.668(1)	-1.734(1)	6.099(-1)	2.972(1)	-1.740(1)	3.855(-1)
5p11Ax1	3.442(1)	-1.715(1)	4.745(-1)	3.616(1)	-1.734(1)	4.108(-1)	3.920(1)	-1.747(1)	2.772(-1)
6p5Ax1	3.941(1)	-1.702(1)	2.804(-1)	4.274(1)	-1.731(1)	2.656(-1)	4.564(1)	-1.754(1)	2.064(-1)

Table 7. Same as Table 5, but now for the J , H , and K bands.

Model	J			H			K		
	t_{rise} [d]	Max. [mag]	ΔM_{15} [mag]	t_{rise} [d]	Max. [mag]	ΔM_{15} [mag]	t_{rise} [d]	Max. [mag]	ΔM_{15} [mag]
3p65Ax1	2.751(1)	-1.731(1)	4.328(-1)	3.041(1)	-1.751(1)	2.992(-1)	2.862(1)	-1.764(1)	4.406(-1)
5p11Ax1	3.786(1)	-1.746(1)	3.279(-1)	3.977(1)	-1.772(1)	2.557(-1)	3.668(1)	-1.768(1)	3.500(-1)
6p5Ax1	4.655(1)	-1.752(1)	2.208(-1)	4.769(1)	-1.777(1)	1.514(-1)	4.610(1)	-1.776(1)	2.127(-1)

itors have surface radii of $\lesssim 20 R_{\odot}$, which causes the faintness of the post-breakout phase relative to the subsequent peak.

The SNe IIB/Ib/Ic models systematically brighten a few days after explosion; this stems from energy deposited into the ejecta by the decay of ^{56}Ni exclusively (other unstable isotopes are ignored in this work). The three models have $\approx 0.09 M_{\odot}$ of ^{56}Ni and radiate about the same amount of energy. They do so over a longer time for higher mass ejecta, and consequently reach a smaller maximum luminosity. For our model set, the rise time to bolometric maximum increases from 26.3 d for model 3p65Ax1 to 41.9 d for model 6p5Ax1, while the peak luminosity drops from 1.65 to 1.49×10^{42} erg s^{-1} , in the same model order.⁴

The post-maximum bolometric light curve shows a more rapid fading for smaller mass ejecta (i.e., 0.61 mag for model 3p65Ax1, and only 0.22 mag for the higher mass model 6p5Ax1). For a higher ejecta mass there is more efficient trapping of stored energy (primarily in the form of moderate-energy “thermal” photons) within the ejecta, as well as more efficient trapping of the γ -rays released by the decay of ^{56}Ni and ^{56}Co . The latter becomes more evident as time progresses. At 140 d past maximum, the bolometric light curve drops at 0.0196 mag per day for model 3p65Ax1, 0.0178 mag for model 5p11Ax1, and 0.0153 mag for model 6p5Ax1.

3.2 Peak bolometric luminosity and ^{56}Ni mass

In our three models the peak luminosity is $\approx 50\%$ larger than the instantaneous decay rate at maximum, significantly offset from the prediction of Arnett’s rule (which states that the bolometric luminosity is equal to the total decay rate at that time; Arnett 1982). This “rule”, identified in a simplified analytical model of SN Ia light curves, is not a fundamental law that should hold exactly because, for example, of energy conservation. There is thus no fundamental reason why it should apply accurately to type Ibc SNe. In the delayed-detonation models of Blondin et al. (2013), which cover a range of ^{56}Ni masses, the offset is up to $\approx 10\%$, and Arnett’s rule

yields a reliable estimate of the ^{56}Ni mass. However, for the models presented here, Arnett’s rule overestimates the ^{56}Ni mass by 44%, 53%, and 52% for models 3p65Ax1, 5p11Ax1, and 6p5Ax1, respectively.

To estimate the ^{56}Ni mass from the bolometric luminosity, one may instead use the idea of Katz et al. (2013), which is robustly based on an energy-conservation argument. Considering heating from radioactive decay and cooling through expansion and radiation, one can solve the internal energy equation out to late times to find

$$tE(t) - t_0E(t_0) = \int_{t_0}^t dt' t' L_{\text{dec}}(t') - \int_{t_0}^t dt' t' L_{\text{bol}}(t') ,$$

where $L_{\text{dec}}(t)$ is the decay luminosity and $E(t)$ is the total radiation energy trapped within the ejecta at t . At late times, as the ejecta becomes optically thin, there is essentially no stored radiation energy so we neglect the term $tE(t)$. To test this expression, we use $t_0 = 3$ d. At that time, E is of the order of 10^{48} erg, and is about a tenth of the time-integrated bolometric luminosity. Furthermore, as expected, the ratio

$$\int_{t_0}^t dt' t' L_{\text{bol}}(t') / \left(\int_{t_0}^t dt' t' L_{\text{dec}}(t') + t_0E(t_0) \right)$$

is within a few percent of unity (a superior accuracy than achieved with Arnett’s rule) at 10–20 d after maximum (Fig. 3). Neglecting the term $t_0E(t_0)$ increases the offset by a few per cent. At early times, the ratio is much below unity because the decay energy is deposited at large optical depth, too large to influence the rate at which radiation escapes from the photosphere. At late times, the ratio drops below unity again because of γ -ray escape — the value of unity would be recovered if we used the decay energy effectively deposited within the ejecta, or if we included the escaping γ -ray luminosity in the bolometric luminosity. At 10–20 d after maximum, γ rays are fully trapped in typical SNe IIB/Ib/Ic and so the relation holds satisfactorily without any detailed calculation at that time. The downside of this approach, which also affects Arnett’s rule (although only at maximum), is the difficulty of constraining the bolometric luminosity from limited multi-band photometry.

⁴ If we scale the peak luminosity to exactly the same ^{56}Ni mass of $0.0742 M_{\odot}$, the peak luminosity drops from 1.65 to 1.12×10^{42} erg s^{-1} .

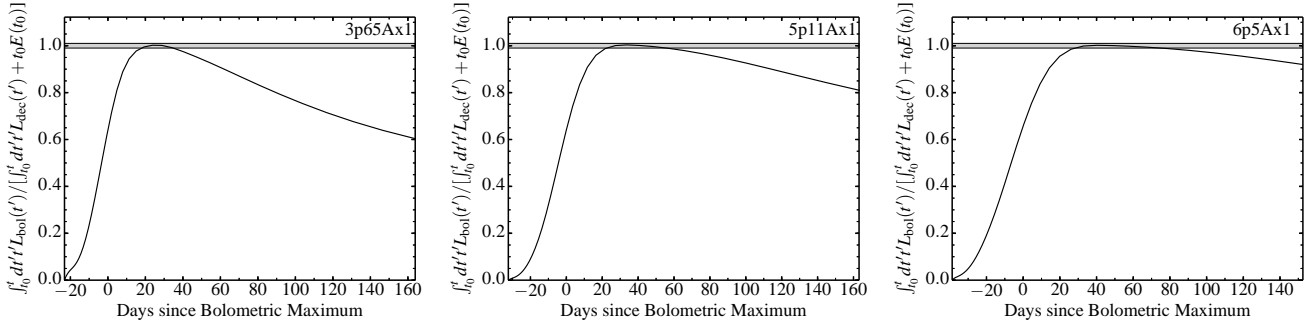


Figure 3. Illustration of the variation of the ratio $\int_{t_0}^t dt' t' L_{\text{bol}}(t') / [\int_{t_0}^t dt' t' L_{\text{dec}}(t') + t_0 E(t_0)]$ versus time since bolometric maximum (we use $t_0 = 3$ d). As pointed out by Katz et al. (2013), this ratio eventually approaches unity at late times if one uses the trapped decay energy. Since the trapped fraction is not directly inferred, we find more convenient to check this expression using the total decay energy. In that case, the ratio is unity to within a few per cent about 10–20 d after maximum. At later times, γ -ray escape makes this ratio drop below unity, the more so as time passes and the ejecta thins out. Higher mass ejecta exhibit a longer period in which the ratio sustains its maximum value.

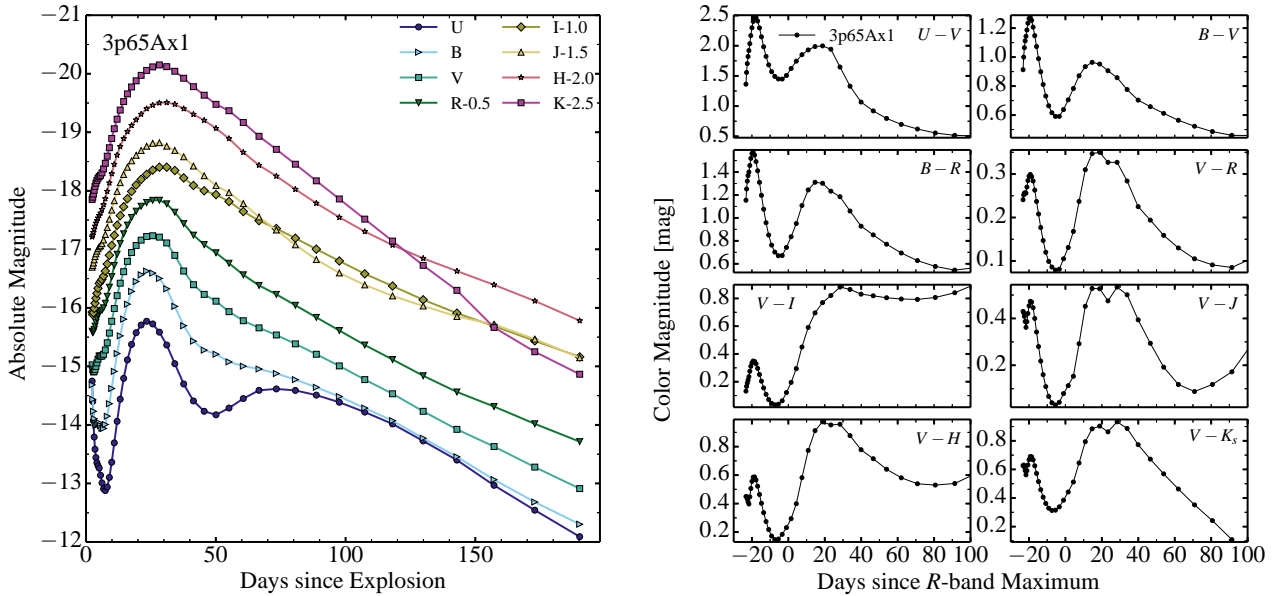


Figure 4. Multi-band light curves (left) and colour evolution for a selection of optical and near-IR bands (right) for model 3p65Ax1. Redder bands tend to peak at later times while the colour evolution shows a complex behaviour. Notice how the minimum colour, for each plotted filter combination, occurs prior to R -band (and hence bolometric) maximum.

3.3 Multi-band light curves

In this section, we use multi-band light curves to discuss the distribution of the emergent flux with wavelength and time. Results, including colours, are shown in Figs. 4–6, while rise times, peak magnitudes, and post-maximum decline rates (the change in magnitude 15 d after the time of peak) are provided in Tables 5–7.

Generally we obtain shorter rise times in bluer optical bands, although an exception is that the I -band peaks later than the J band (likely because of the strengthening Ca II triplet lines; see Section 4). The R band peaks within about a day of the bolometric light curve maximum. As for the bolometric maximum, models with a larger ejecta mass peak later. Higher mass models also show a larger spread in the times at which each magnitude peaks. Because of the comparable ^{56}Ni mass, the peak magnitudes are, however, similar, band-by-band, for all three models. For example, we obtain a peak R band magnitude of -17.34 , -17.34 , and -17.31

for models 3p65Ax1, 5p11Ax1, and 6p5Ax1 (a closer correspondence than for the bolometric luminosity maximum).

A similar behaviour is seen in SN Ia models (see, e.g., Blondin et al. 2015) and in both cases results from a combination of effects. On the rise to maximum, the ejecta heats up and the emissivity at depth shifts to shorter wavelength — this is in part reflected by the behaviour of the electron-scattering photosphere (Fig. 7). The ejecta is thus not expected to evolve at constant colour. However, line blanketing causes strong energy redistribution to longer wavelength. As we approach the bolometric maximum, lines strengthen (see also Section 7), dominating the emissivity and the opacity over continuum processes. The magnitude of the effect grows with time as the spectrum forms deeper into more metal-rich regions.

Past maximum, the decline rates are greater in bluer optical bands, and the more so for lower mass models — $\Delta M_{15} = 1.17$ mag

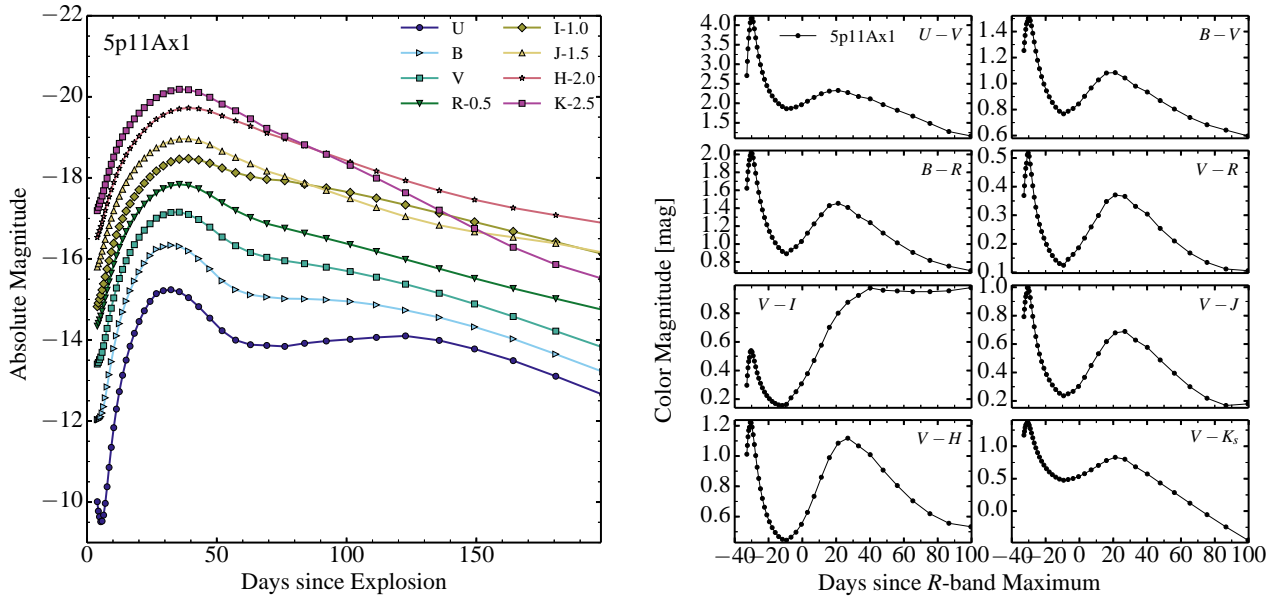


Figure 5. Same as Fig. 4, but now for model 5p11Ax1.

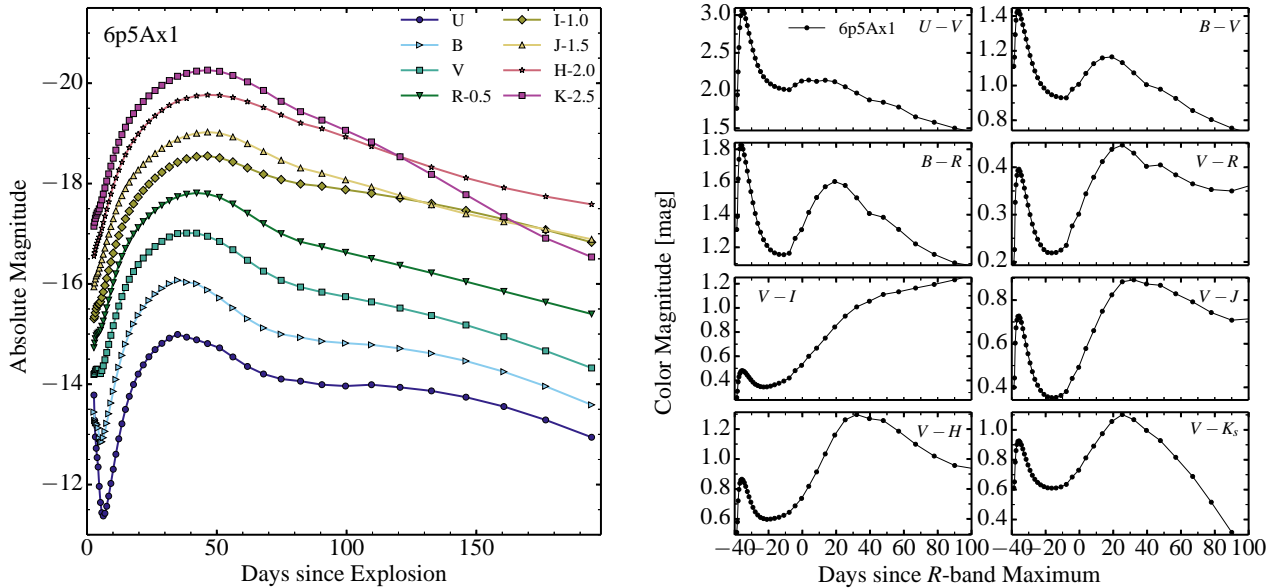


Figure 6. Same as Fig. 4, but now for model 6p5Ax1. The curves are similar to those shown for model 3p65Ax1, but the timescales for the variations are longer.

in the U band for model 3p65Ax1, but only 0.25 mag for model 6p5Ax1. In the higher mass model 6p5Ax1, the decline rate over 15 d in different bands shows much less scatter than for the lighter model 3p65Ax1, which reflects the longer diffusion time of the former.

The colour evolution for all three models is qualitatively similar, despite the differences in mass and composition (right panels of Figs. 4–6). During the first few days after explosion, all models become redder. Unfortunately, although there may be a physical effect here, this may in a large part stem from the initial relaxation of

the \checkmark d model into CMFGEN. Subsequently, because of the heat supply from decay, they become bluer on the rise to maximum. From maximum until 20 (model 3p65Ax1) to 40 d (model 6p5Ax1) they become redder, probably because of the increasing effect of blanketing. Beyond that time, as the ejecta turns progressively nebular, the colours become bluer again. At nebular times, the colours reflect in part the distribution of forbidden-line transitions and thus can show great disparity between filter sets.

In our set of models, the initial colours are systematically red, unlike explosions occurring in extended stars — the larger the ini-

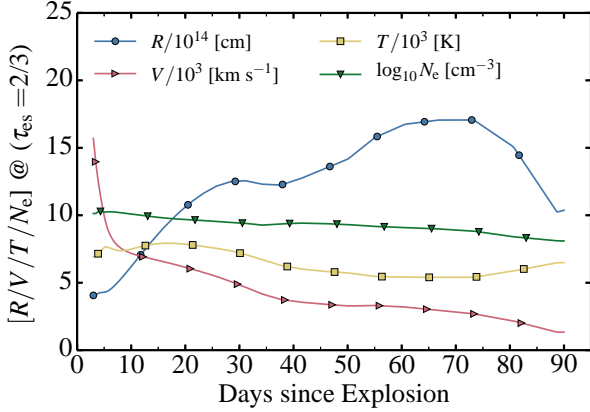


Figure 7. Evolution of the ejecta properties at the electron-scattering photosphere for model 3p65Ax1.

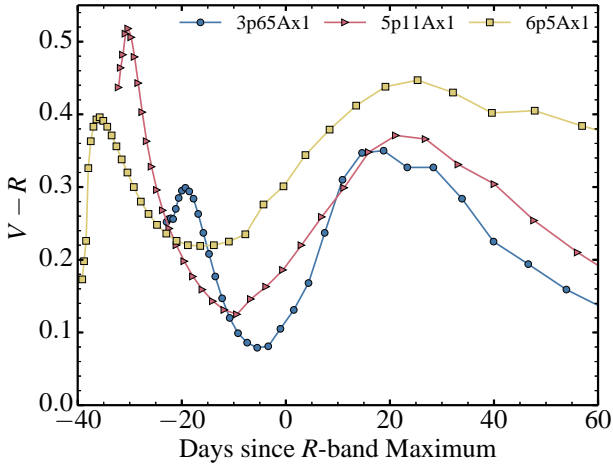


Figure 8. Comparison of the $(V - R)$ light curve for models 3p65Ax1, 5p11Ax1, and 6p5Ax1. At 10 d after R -band maximum, the mean value is 0.322 mag and the standard deviation is 0.047 mag.

tial radius, the bluer the colours at early times and the more delayed the phase of recombination (Dessart et al. 2013a). This is a bias in our sample of progenitors, which is limited to close-binary systems in which the primary star explodes with a final radius $\lesssim 20 R_{\odot}$.

Drout et al. (2011) reported a small scatter of 0.06 mag about a mean $(V - R)$ colour of 0.26 mag at 10 days after V -band maximum for observed SNe I Ib/Ic with an inferred reddening. In our models, we also find that the colours early after peak are comparable. For $(V - R)$ at 10 d after R -band maximum, we obtain a mean of 0.32 mag, with a standard deviation of 0.04 mag (Fig. 8). The larger sample of models also shows this behaviour, with a similar mean (the standard deviation is reduced if we limit the sample to lower-mass ejecta; Dessart et al., in prep.). This uniformity in post-maximum colour can thus be used to constrain the reddening in SNe I Ib/Ic.

While the bolometric correction can be estimated for our models for any band, a more accurate estimate of the bolometric luminosity can be obtained by using multiple passbands. Here we extract the relative fraction of the flux that falls within the UV, the op-

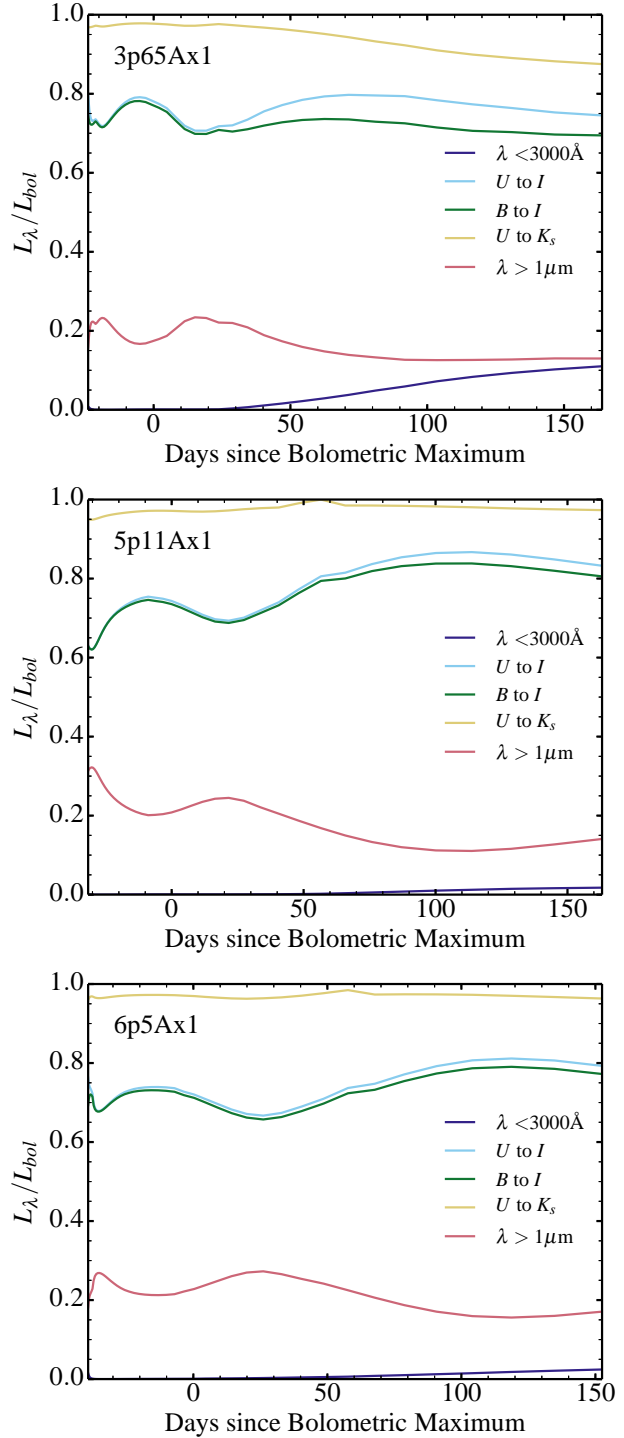


Figure 9. Fractional flux falling into different spectral regions for the models 3p65Ax1, 5p11Ax1, and 6p5Ax1 up to about 200 d after explosion.

tical and the near-IR (Fig. 9). Because of the cool “photospheric” temperature of our model (Fig. 7), and the strong blanketing by lines (see below), the UV is subdominant at all times. The UV rises a little at nebular times, in particular in the lower mass model, but remains sub-dominant. The bulk of the radiation emerges in the optical range ($\approx 80\%$), with the rest at longer wavelengths and primarily in the near-IR — little flux is emitted beyond 2–3 μm .

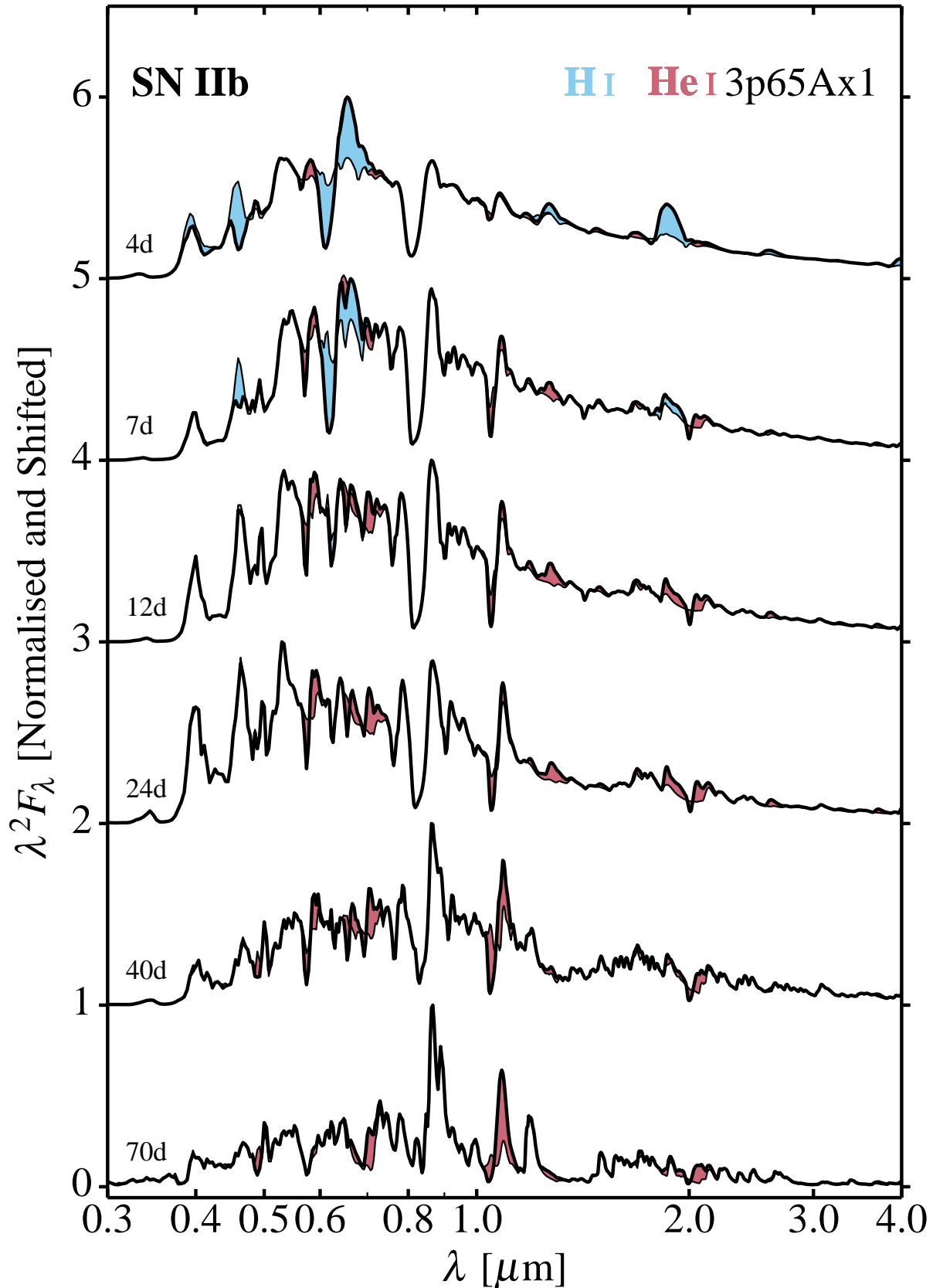


Figure 10. Spectral evolution of model 3p65Ax1 from 0.3 to 4 μm until 70 d after explosion (we show $\lambda^2 F_\lambda$ for better visibility). Overlaid on the full synthetic spectrum (black thick line), we hatch the offset in flux obtained when H I and He I bound-bound transitions are omitted from the formal solution of the radiative transfer equation. The presence of H I and He I lines at early times, and the absence of H I at late times, makes this model a type IIb.

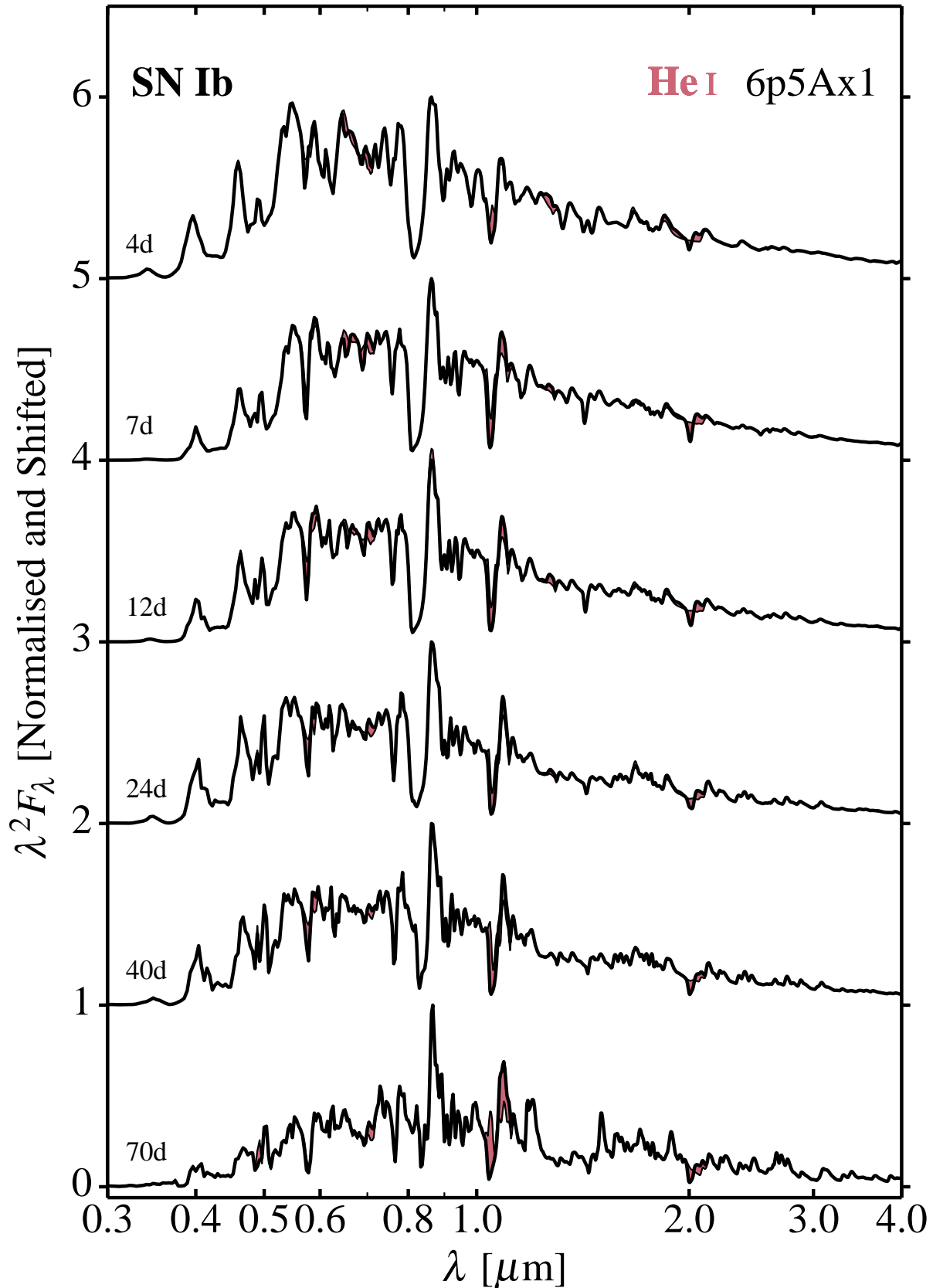


Figure 11. Same as Fig. 10, but now for model 6p5Ax1. H I lines are not plotted since hydrogen is absent in the ejecta. This model corresponds to a Type Ib SN. Even for this model, with a He mass of $1.67 M_\odot$, He I lines (except for $\lambda 10830$ and $\lambda 20580$) are relatively weak and/or blended. At 70 days, and unlike earlier epochs, He I 10830 \AA is almost entirely responsible for the P Cygni profile seen near 10830 \AA .

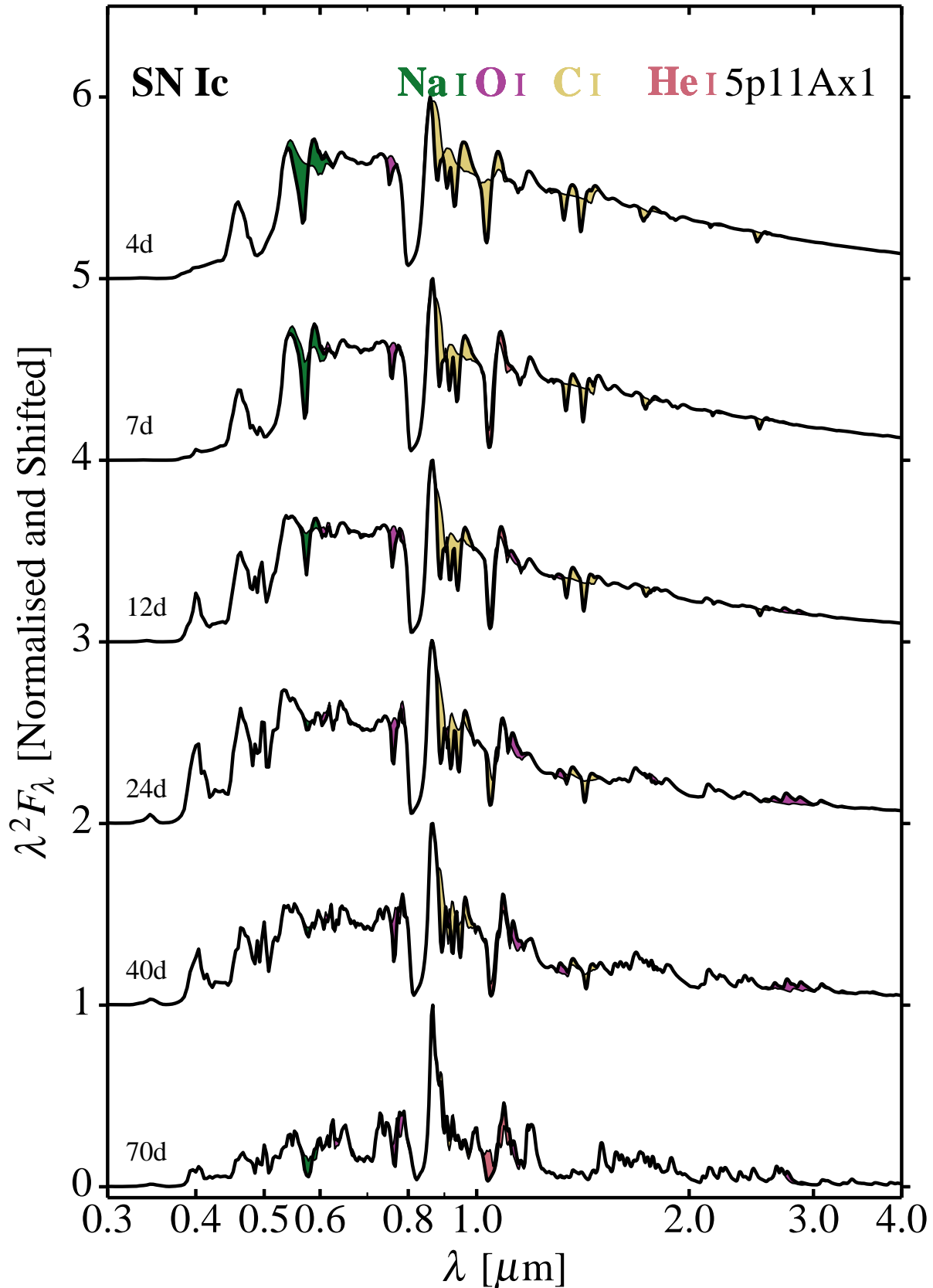


Figure 12. Same as Fig. 11, but now for model 5p11Ax1. Although helium is present in the ejecta, only the He I line at 10830 \AA is visible over the entire optical and near-IR ranges, and only at late times. This model corresponds to a Type Ic SN. At early epochs Na I D could be erroneously identified with He I λ 5876.

4 SPECTROSCOPIC PROPERTIES

4.1 Spectral evolution for our model set

The three models 3p65Ax1, 5p11Ax1, and 6p5Ax1 have the same explosion energy ($\approx 1.2 \times 10^{51}$ erg), a similar ^{56}Ni mass ($\approx 0.09 M_{\odot}$), similar ejecta masses ($2\text{--}5 M_{\odot}$), and small progenitor radii ($\lesssim 20 R_{\odot}$). However, a fundamental distinction between these ejecta is their composition. As shown in Dessart et al. (2011), even $\sim 0.001 M_{\odot}$ of hydrogen can lead to a strong H α line at early times, while even a helium mass fraction of $\sim 30\%$ may produce no He I line (Dessart et al. 2012). Our three models have composition characteristics (see Tables 3 and 4, and Fig. 1) that make them suitable candidates for a type IIb (model 3p65Ax1), a type Ib (model 6p5Ax1) and a type Ic (model 5p11Ax1).

We show the spectral evolution of each model in Figs. 10–12, covering from 4 to 70 d after explosion and over the range 0.3–4 μm . None of our models show blue featureless spectra at early times, likely because the progenitor radii are small so that expansion cooling causes a large drain of internal energy in the outer ejecta layers. To avoid unnecessary speculations, we delay further discussion to a detailed study focused on that aspect alone.

There is a great similarity of the spectral energy distribution for the three models at all times shown, with the bulk of the flux emerging in the optical range and strong signatures of line blanketing by Fe II and Ti II (see below). However, closer examination reveals significant differences. To highlight these differences, and to make more obvious the classification of the model as type IIb, Ib, or Ic, we colour the flux associated with specific ions. This contribution is estimated by excluding the bound-bound transitions of a given ion in the formal solution of the radiative-transfer equation.

Model spectra for 3p65Ax1 exhibit H I lines (primarily H α and H β in the optical, and P α in the near-IR) at early times and up to the peak, while He I lines are present at all times, both in the optical and in the near-IR (Fig. 10). These He I lines may be present early on without the influence of ^{56}Ni decay (Dessart et al. 2011), but non-thermal excitation and ionisation are essential to produce them after a few days (Lucy 1991; Dessart et al. 2012; Hachinger et al. 2012; Li et al. 2012). This is because the temperature in the spectrum formation region is low, so that He I lines cannot be thermally excited. The ionisation of He (and of other species) in the spectrum formation region is low (Fig. 13). We find He I lines at 5875, 6678, 7068, 10830, 11013.07, 12527.5, 12846.0, 12984.9 (and numerous other contributions that overlap around 1.25–1.3 μm), 15083.6 (weak), 17002.5 (weak), 18685.4 and 19543.1 (overlap with P α), 20581.0 (strong) + 21120.2 (and other similar lines that overlap on the red edge of 2.0581 μm), 26881.2 (together with other He I lines that overlap), and 37025.6 \AA . With the presence of H I lines early on and the persistence of He I lines, the 3p65Ax1 model corresponds to a SN IIb.

Model 6p5Ax1 shows a very similar evolution to model 3p65Ax1 but because the ejecta is hydrogen deficient, it shows no H I lines (Fig. 11). This model corresponds to a type Ib SN. Interestingly, the two sequences for the IIb and the Ib models are very similar if we omit the differences made by H I lines. Hydrogen is so under-abundant in model 3p65Ax1 that it does not affect significantly the radiative transfer solution – hydrogen acts only as a trace element.

Model 5p11Ax1 shows the same overall evolution in spectral energy distribution but for this carbon and oxygen rich ejecta the spectral signatures are distinct (Fig. 12). Despite the $0.32 M_{\odot}$ of helium and 30% surface helium mass fraction, He I lines are always absent in the optical. The He I line at 10830 \AA is present at all times,

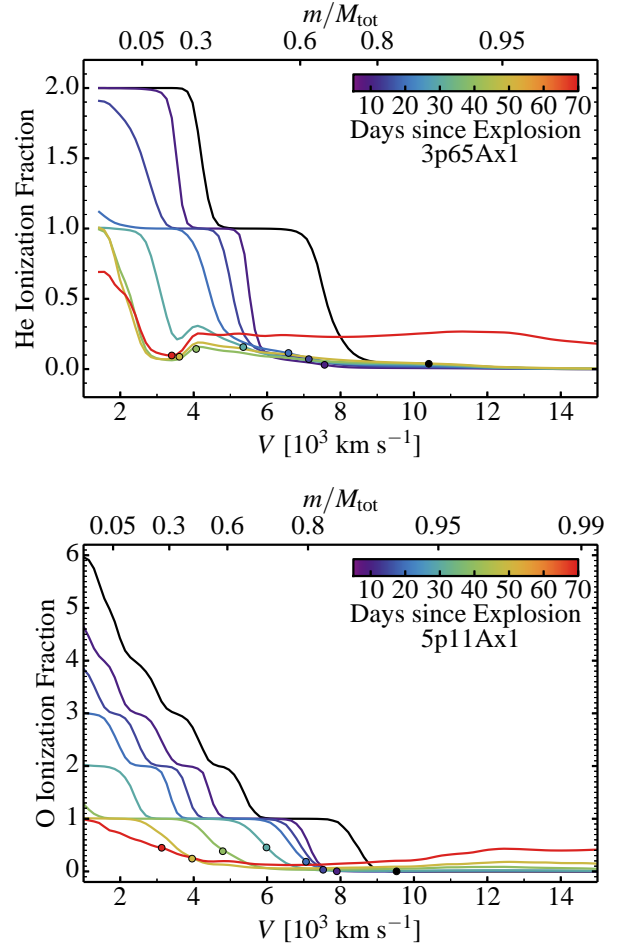


Figure 13. Evolution of the ionisation fraction of He in model 3p65Ax1 (top) and of O in model 5p11Ax1 (bottom). Specifically, the quantity plotted is $\sum_i i N_i / N_{\text{tot}}$, where N_i is the species number density when i -times ionised and N_{tot} is the species total number density. Symbols denote the location of the photosphere (using the Rosseland-mean opacity). The times shown are 4, 6, 8, 10, 15, 20, 30, 40, and 50 d after explosion for the top panel. The times shown are 5, 10, 15, 20, 30, 40, 50, and 70 d after explosion for the bottom panel.

but it is badly blended at early times – absorption that could be erroneously associated with He I alone is also due to C I and Mg II. Paradoxically He I $\lambda 10830$ is strongest at late times (see below). This model is significantly mixed (just like the other two models) and so the lack of He I lines results from the low helium abundance and the large CO core mass (Dessart et al. 2012).

The buffer of mass lying in between the ^{56}Ni rich layers and those rich in helium is much larger in model 5p11Ax1, preventing efficient non-thermal excitation at early times. Model 5p11Ax1 exhibits an extended oxygen-rich shell, whose outer part is rich in carbon and poor in helium (mass fraction of 10%). In contrast, in models 3p65Ax1 and 6p5Ax1, the oxygen shell is less massive and resides underneath a massive helium-rich shell ($>90\%$ mass fraction helium). This difference in core structure stems from the difference in main sequence mass. Models 3p65 and 6p5 stem from stars with initial masses 16 and $25 M_{\odot}$, which make a relatively small CO core compared to model 5p11 which stems from a star with an initial mass of $60 M_{\odot}$ that eventually formed a massive CO core. All else being the same (^{56}Ni mass, mixing magnitude, ex-

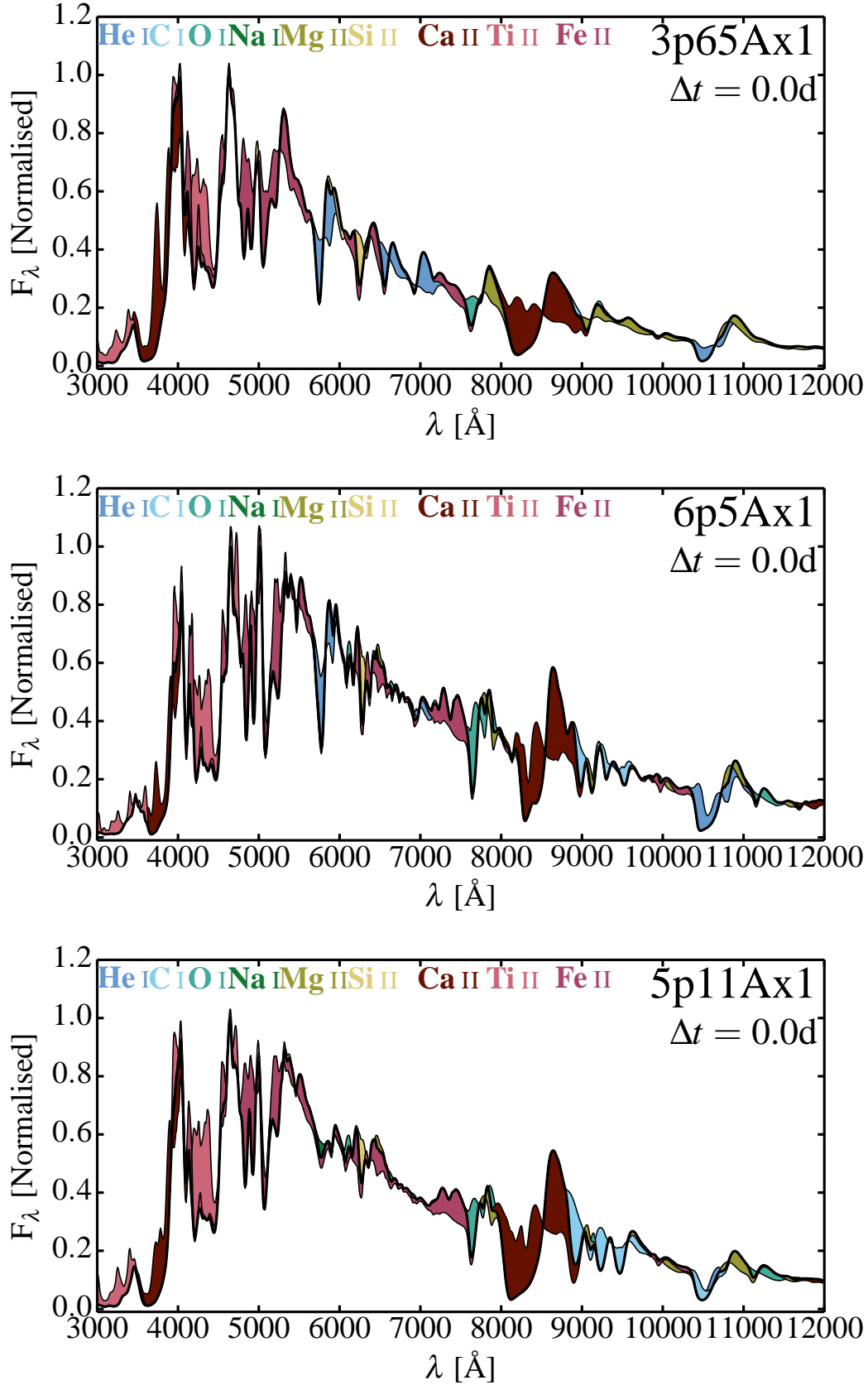


Figure 14. Maximum light optical spectra for models 3p65Ax1 (SN IIb), 6p5Bx1 (SN Ib), and 5p11Ax1 (SN Ic). We illustrate the contributions from lines of different ions by colouring the space that separates the full spectrum (dark black curve) from that obtained by neglecting a given ion from the formal solution of the radiative-transfer equation.

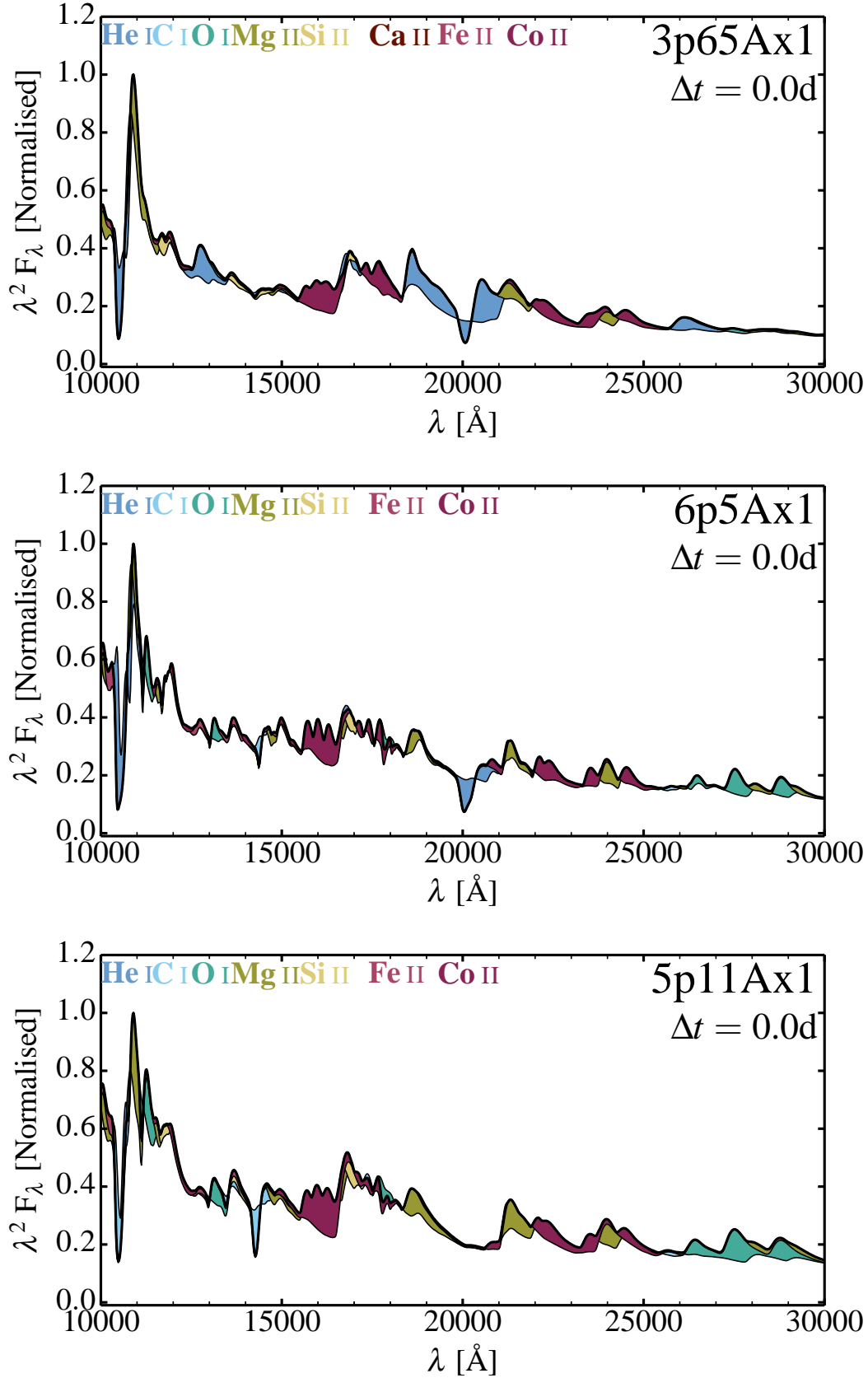


Figure 15. Same as Fig. 14, but now for the near-IR range. For better visibility, we show the quantity $\lambda^2 F_\lambda$.

plosion energy), this difference in core structure causes the lack of He I signatures in model 5p11Ax1. In this SN Ic model, the feature at 5900 Å is solely due to Na I D (strong at early and late times but weak around maximum).

Our result disagrees somewhat with Hachinger et al. (2012) who find in their study that as little as 0.14 M_{\odot} of He may suffice for the production of He I lines. There is probably no clear threshold because the excitation of He I lines will depend not just on He abundance, but also on ^{56}Ni mass, mixing, the size of the CO core, and the C and O mass fraction in the outer parts of the progenitor.

Iron group elements have a mass fraction equal to the progenitor metallicity value throughout the ejecta except in the innermost layers (with the exception of ^{56}Ni and its daughter nuclei). Here, iron-group elements cause blanketing in the optical (Fe II, Ti II) and in the UV (Ti II). Numerous lines from Co II produce a broad emission feature at 1.6 μm . Because of steady burning within the progenitor helium core, intermediate mass elements have abundances that are over- or under-abundant compared to solar, with variations between models and also with depth for each model.

In the type Ic model, most of the features between 9000 Å and $\approx 1\mu\text{m}$ are due to C I, while these features are very weak in the Type IIb model 3p65Ax1. In the type Ib model 6p5Ax1, these C I lines are visible around maximum and later because of the larger CO-rich shell in this more massive progenitor. Hence, C I lines offer a possible diagnostic if the identification of He I lines is ambiguous – a strongly He-rich photosphere would most likely exhibit weak or no C I lines in the 9000 Å and $\approx 1\mu\text{m}$ region.

Oxygen shows only one signature in the optical with O I 7777 Å. This feature is strong at all times in model 5p11Ax1 but its presence in the type IIb model 3p65Ax1 likely results from mixing (the helium-rich shell is strongly deficient in oxygen in the pre-SN model). Improving our current algorithm for mixing is work in progress — while ^{56}Ni may be mixed far out in the ejecta, intermediate mass elements may not (Wongwathanarat et al. 2014).

Na I D is conspicuous only in the type Ic model, and could be confused with He I 5876 Å. Neon lines are absent at all times and in all models. Magnesium lines stem primarily from Mg II. In the optical, we predict (usually blended) lines at 7790, 8213–8234, 9218–9244, 10910, 21368–21432, 24042–24124 Å. In model 3p65Ax1, these lines are probably present even at early times because we mix magnesium out in velocity space (O, Ne, Mg are originally under-abundant in the He-rich shell).

Lines from Ca II (H&K lines and the triplet at 8500 Å) are strong at all times, and of comparable strength in the three models. Being closely tied to the ground state (directly or through Ca II H&K for the triplet), these lines are strong even at solar abundance so they provide little constraint to help distinguish different ejecta.

All these signatures are illustrated at the time of bolometric maximum for the optical range in Fig. 14 and for the near-IR range in Fig. 15. These figures are merely for illustration, not quantitative estimates, since excluding a given ion in the computation of the spectrum breaks the consistency of the calculation.

5 NEAR-IR He I LINES

The identification of He I lines in SN Ib/c spectra is a recurring issue in the SN community. The problem is overemphasised since helium is likely present in all core-collapse SNe, simply in different abundances. For example, optical He I lines are seen in Type II SN spectra only prior to hydrogen recombination. During the rest of

the photospheric phase, optical He I lines are absent although about 30% of the total hydrogen-envelope mass is helium (Dessart et al. 2013b). In that case, there is little debate about the presence of helium because hydrogen is present, although the difficulty in producing He I lines in such cool atmospheres is already evident.

In hydrogen poor ejecta, the same issue returns, but here the problem is whether the SN atmosphere lies within the He-rich shell ($\gtrsim 90\%$ helium mass fraction) or within the CO core (typically $\lesssim 10\%$ helium mass fraction). Hence, the production of He I lines depends on the ejecta composition. Furthermore, the need for non-thermal excitation/ionisation represents a major hurdle. Any ejecta with a massive CO core will probably never show strong He I lines because of the large mass buffer between the ^{56}Ni rich regions and the outer He-rich regions (whose presence is not even guaranteed because of mass loss). This suggests that SNe IIb/Ib progenitors preferentially arise from lower mass progenitors (which have small CO cores), where even moderate mixing can foster the production of He I lines (Dessart et al. 2012).

In this section, we document the properties of two spectral regions notorious for their possible He I signatures, at 10830 Å and 20581 Å (Figs. 16–18). He I 10830 Å is the strongest line, and has the potential to confirm or deny the presence of He in SN Ic. Filippenko et al. (1995) used the presence of strong absorption near 10830 Å to argue for the presence of He in the Type Ic SN 1994I. Later work by Millard et al. (1999) found, using the parameterised synthesis code SYNOW, that the feature could not be fitted by He I alone. They suggested that it was a possible blend with C I. Later work by Sauer et al. (2006) confirmed this suggestion. Other studies (e.g., Meikle et al. 1996; Hachinger et al. 2012) show that Mg II is also a possible contributor.

In type IIb/Ib models 3p65Ax1 and 6p5Ax1, the 10830 Å region is dominated by the He I line, with a modest contribution of Mg II 10914 Å (multiple transitions), and O I 11300 Å in the red wing (multiple transitions). At late times, numerous lines from Ca II, Fe II, and Co II appear around 1 μm and affect the blue wing of the He I line. In model 5p11Ax1, similar features are present, but with the addition of a strong overlapping component from numerous C I transitions around 10700 Å. Around bolometric maximum, the He I contribution to the 10900 Å feature is weak relative to that of C I and Mg II. However, it is still important. To remove the feature seen near 10900 Å we would need to simultaneously omit He I, C I, and Mg II lines from the spectrum calculation. The relative strength of these different contributions varies with time, and He I is a significant component at all times only in the type IIb/Ib models.

In the 20581 Å region, the dichotomy between SNe IIb/Ib and SNe Ic is more evident. Indeed, He I 20581 Å is present in our type IIb/Ib models but completely absent in the type Ic model. Because there are no other lines at that location, the lack of a feature there is clear evidence that there is no He I line. Hachinger et al. (2012) also highlight the importance of the He I 20581 Å line in assessing the He abundance of SN Ib/c ejecta. Note that in our SNe IIb/Ib models, there are He I lines around 1.9 μm (e.g., 19543.1 Å), which spread the influence of He I far to the blue of the 2.0581 μm feature.

An interesting feature of our simulations, also observed (see, e.g., Ergon et al. 2014 for SN 2011dh), is the migration of the location of maximum absorption (or more generally the broadening) of the He I lines at 10830 and 20581 Å. This is the spectral counterpart of the rapid photometric decline at late times. Indeed, before γ rays start to escape, they first deposit their energy non locally within the ejecta, increasingly influencing the outer layers after bolometric maximum. When this effect arises, non-thermal excitation and ion-

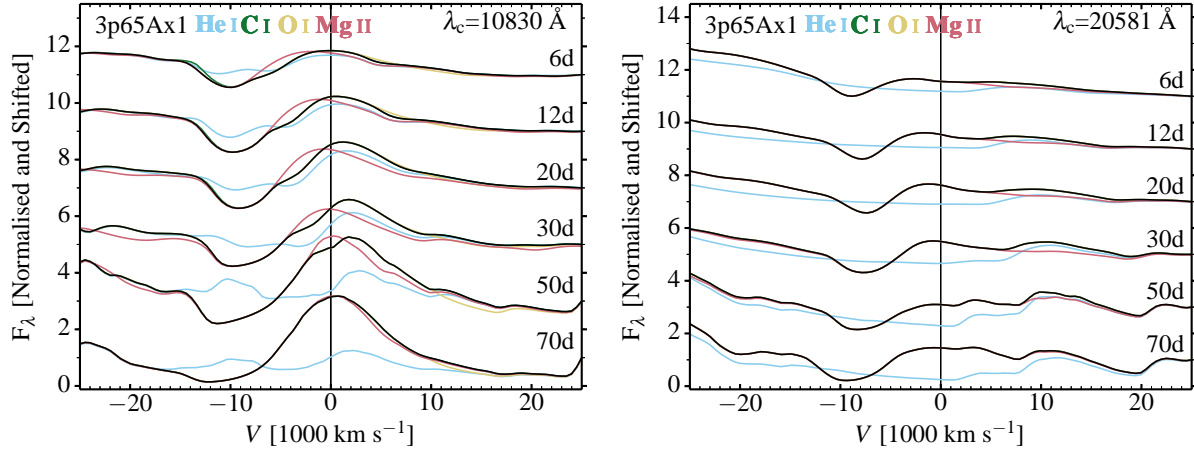


Figure 16. Illustration of the 10830 and 20581 Å regions for model 3p65Ax1 (type IIb). We show the contributions from He I, C I, O I, Mg II lines to highlight the fractional importance of each species/ion. In these IIb spectra, high velocity absorption (around $-10,000 \text{ km s}^{-1}$) associated with both 10830 and 20581 provides unambiguous evidence for the presence of He. However, even in this case Mg II has a significant influence on the emission component of 10830 Å.

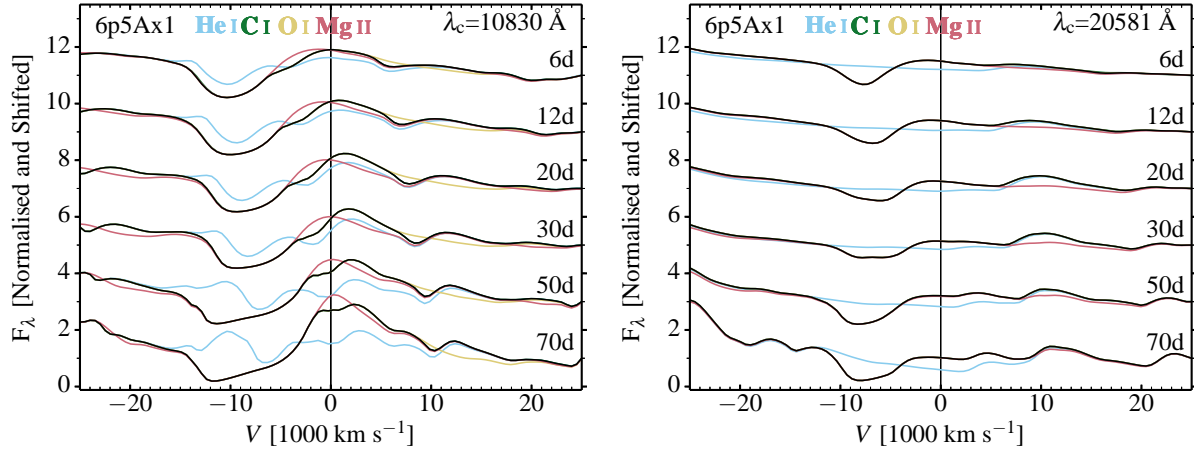


Figure 17. Same as Fig. 16, but now for model 6p5Ax1 (type Ib). He I 20581 Å is present at all times, and hence provides a very useful diagnostic of the presence of helium.

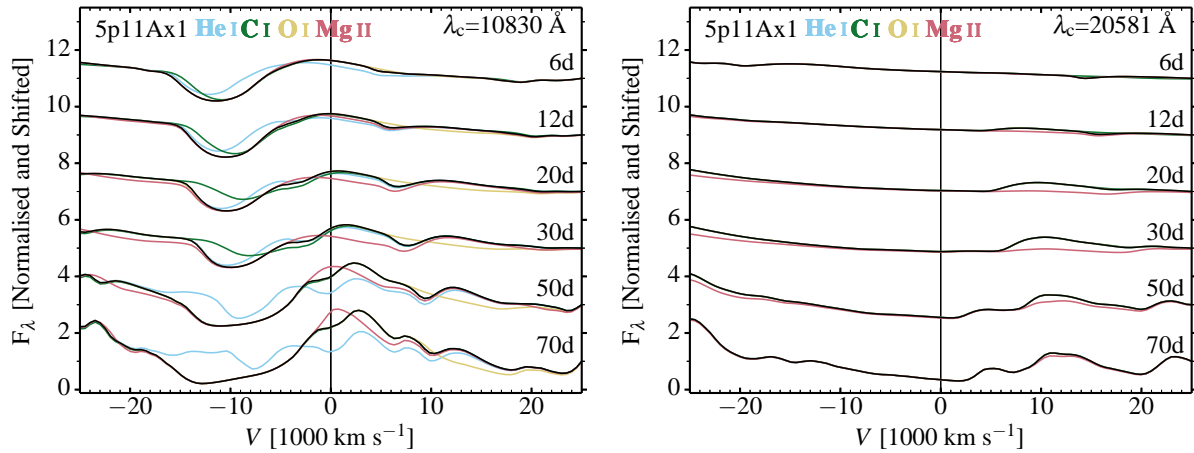


Figure 18. Same as Fig. 17, but now for model 5p11Ax1 (type Ic). Notice the complicated blend associated with the P Cygni profile at 10830 Å while there is a firm non-detection of He I at 20581 Å. At late times the 10800 Å feature shows high velocity absorption (beyond $-10,000 \text{ km s}^{-1}$) that is only associated with He I 10830 Å.

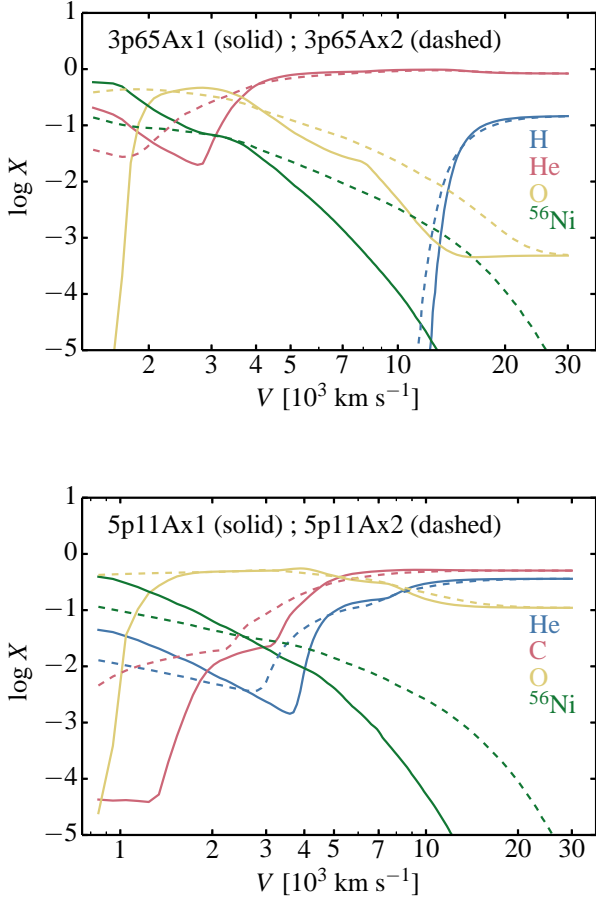


Figure 19. Ejecta composition profiles for models 3p65A (top) and 5p11A (bottom) with moderate (x1) and strong (x2) mixing. [See Sections 2 and 6 for discussion.]

isation processes are boosted in the outer ejecta layers (which are poor in ^{56}Ni initially), increasing the optical depth in these strong He I lines. In type Ic model 5p11Ax1, only the He I contribution to the 10900 Å feature shows this behaviour, which may serve as a tracer of helium in the ejecta.

6 INFLUENCE OF MIXING

In Dessart et al. (2012), we performed controlled experiments on the effect of mixing in He-rich low-mass ejecta models. This study emphasised how the distribution of ^{56}Ni is critical for the production of He I lines. Indeed, even in ejecta abundant in helium, weak mixing would lead to a type Ic SN. The existence of SNe IIb/Ib is a robust indication that extensive (macroscopic) mixing takes place in these explosions, and by extension, is a likely feature of all core-collapse SNe.⁵

The production of He I lines and a type Ib SN requires both the presence of a large helium mass and a strong mixing of ^{56}Ni

⁵ We note that, theoretically, He I lines may be present at the earliest times without the influence of non-thermal effects, but their presence in this case is very short lived and limited to progenitors with a He-rich shell (for a discussion, see Dessart et al. 2011).

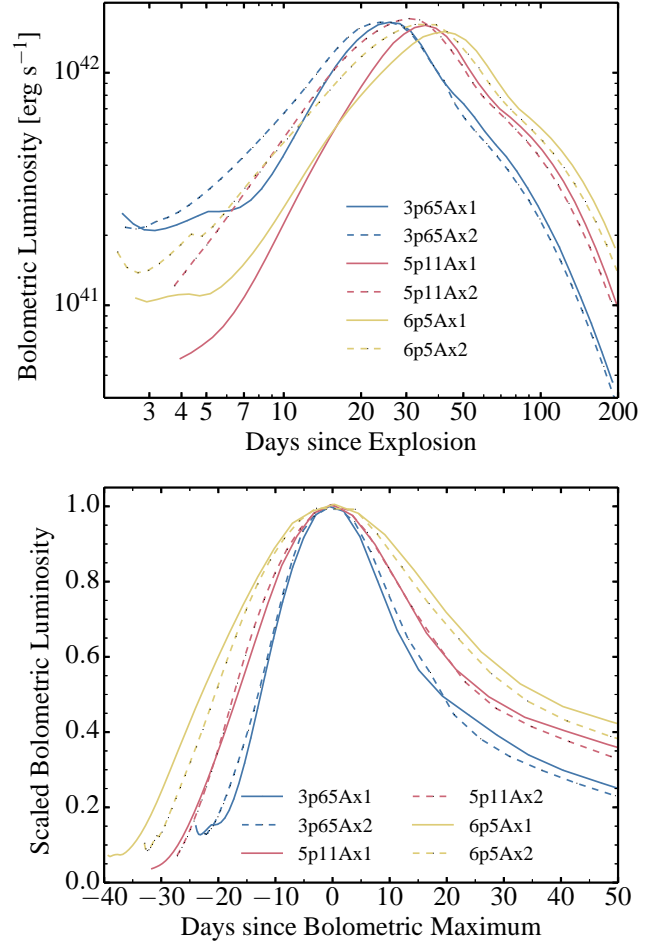


Figure 20. *Top:* Illustration of the effect of a variation in the magnitude of mixing (x1 versus x2, i.e., moderate versus strong mixing) on the bolometric luminosity light curve for our three ejecta models. *Bottom:* Same as top, but now showing the bolometric light curves normalised to their maximum value and shifted so that the origin is the time of bolometric maximum.

into the He-rich layers. This implies that any progenitor star characterised by a large CO core would tend to form a SN Ic because the He-rich regions are too remote from the inner ejecta where ^{56}Ni is produced. It is likely that mixing is a ubiquitous feature of core-collapse SNe. The details and degree of mixing as a function of progenitor and explosion properties are, however, uncertain.

In the present work, all models have therefore been mixed. From our set of models, we indeed produce type IIb/Ib and Ic SNe for the reasons described above. But to quantify the uncertainties associated with mixing, we run strongly-mixed counterparts to models 3p65Ax1, 5p11Ax1, and 6p5Ax1 — these strongly mixed models are given the suffix x2. Our mixing procedure at present applies to all species and is thus indiscriminate (Fig. 19). In contrast, models without mixing would show shells with nearly 100% ^{56}Ni mass fraction in the innermost layers of the ejecta and none above, as in the (unmixed) models studied in Dessart et al. (2012).

As is well known, stronger mixing causes a higher luminosity (e.g., Bersten et al. 2012) and bluer colours (Dessart et al. 2012) at early times. The larger amount of ^{56}Ni at larger velocities causes enhanced escape as time progresses, causing a lower luminosity after maximum. In all three models, mixing causes the maximum to shift to earlier times, with the largest shift occurring for the high-

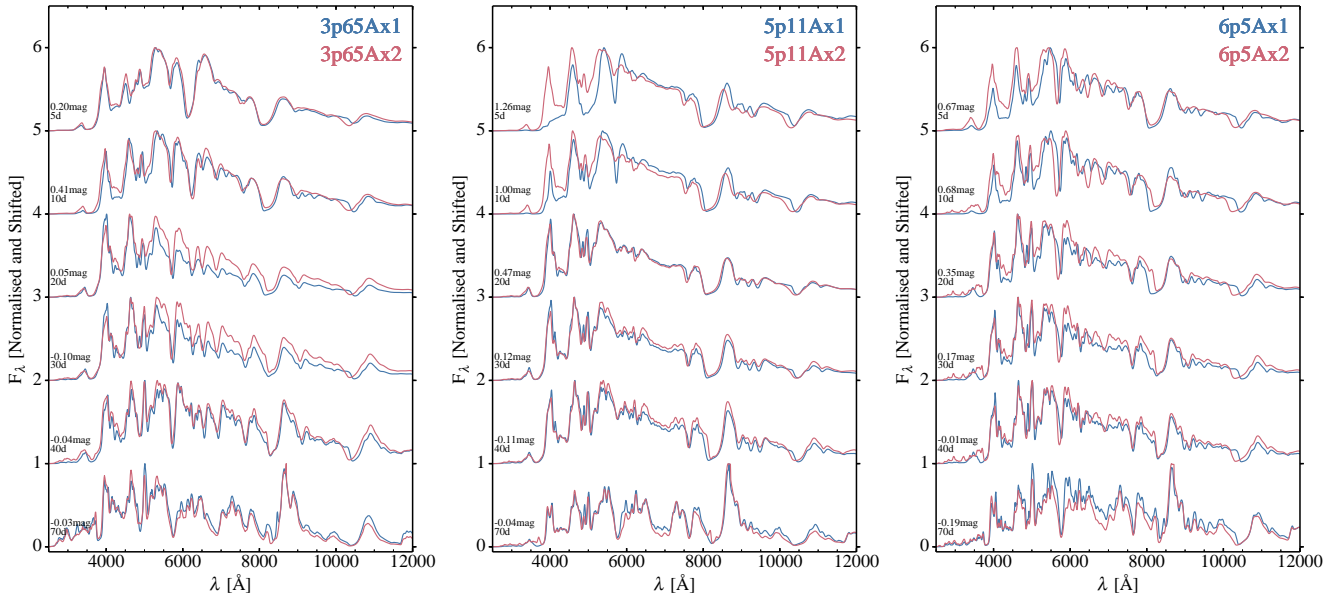


Figure 22. Illustration of the impact of mixing on the spectral evolution of our three models. Each pair corresponds to ejecta with a moderate (x1) and a strong (x2) mixing. Labels provide the time since explosion as well as the magnitude offset between the two models at each date. Besides the impact on the bolometric luminosity and colour, stronger mixing boosts non-thermal processes and leads to broader lines (at fixed E_{kin} and M_e). The effect is therefore more evident on He I lines.

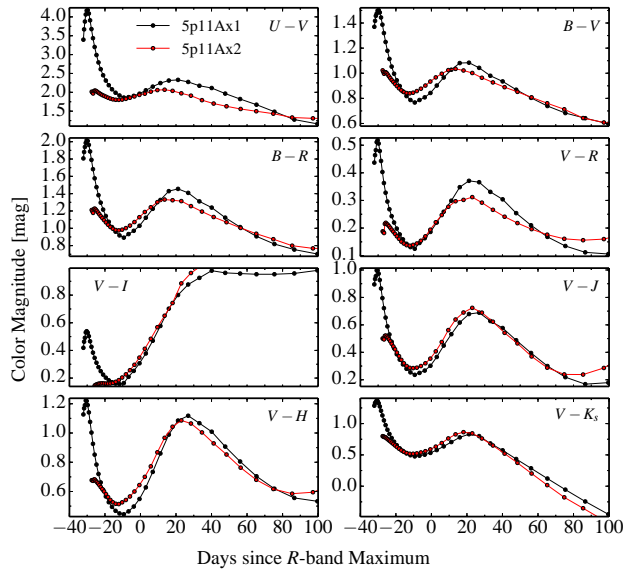


Figure 21. Illustration of the impact of mixing on the colour evolution of model 5p11A. Time is given in days since R -band maximum. Model with suffix x1 has weaker mixing than model with suffix x2 (see Fig. 19 for the composition profiles).

est mass ejecta (Fig. 20). For 3p65Ax1/x2 the shift is 1.4 d, for 5p11Ax1/x2 it is 5.0 d, and for 6p5Ax1/x2 it is 6.7 d. For model 6p5Ax2 the maximum bolometric luminosity is about 10% larger compared to the model with the lower mixing; for the other models the change is even smaller. When we use the time of bolometric maximum as the time origin, the curves for the moderately mixed and strongly mixed models show a remarkable similarity for the two models with the lowest ejecta mass – the bolometric light curve for 6p5Ax2 is somewhat broader (by about a week at 50% maximum) than the light curve for 6p5Ax1 (Fig. 20). This morpholog-

ical similarity for different mixing means that the explosion date could be in error by as much as a week if only the bolometric light curve was used.

In our procedure, mixing enhances the mean atomic weight of the outer ejecta layers. While this should strengthen line blanketing, we observe bluer colours in strongly mixed models because of the extra heating from ^{56}Ni decay (Fig. 21). After maximum, the colour offset due to different mixing is much weaker. For $(V - R)$ at 10 d past R -band maximum, the offset is negligible.

Synthetic spectra corroborate these properties but also illustrate how stronger mixing leads to broader lines (see also Dessart et al. 2012), even at fixed ejecta mass and kinetic energy (Fig. 22). The effect is particularly visible on He I lines and directly stems from the modulation of the magnitude of non-thermal processes — SN Ic spectral line profiles are less sensitive to mixing in that respect. Uncertainties in the mixing magnitude in SNe Ib introduces an uncertainty in the inferences on the explosion energy, ejecta mass etc.

The impact of mixing is greater in higher mass ejecta models like 5p11Ax1 and 6p5Ax1 because mixing is the only way the outer ejecta can be influenced by non-thermal processes. In lower mass ejecta, like model 3p65Ax1, strong mixing is less critical because the outer ejecta (basically the He-rich shell) is close to the ^{56}Ni rich layer – it is only separated by a thin O-rich layer.

7 THE AMBIGUOUS NOTION OF A PHOTOSPHERE

For stellar work, the photosphere is usually defined to be the location at which the Rosseland-mean optical depth is $2/3$, a definition which follows from the Eddington-Barbier relation for a plane-parallel atmosphere (e.g., Mihalas 1978). For extended atmospheres a more practical relation might be the atmospheric location where the probability of photon escape is 50%, or alternatively, that location beyond which 50% of the observed flux originates. Unfortunately, because the opacity has a strong wavelength-dependence,

and because of the rapidly expanding ejecta, the photosphere is not uniquely defined, and even at a single wavelength photons will escape over a region which is spatially extended. The strong effect of line blanketing in the UV increases the effective photospheric radius for bluer photons, while redder photons in the optical, decouple from the gas at a radius comparable to the Rosseland-mean or flux-mean photosphere (Fig. 23). Still, even within the optical, this decoupling radius can vary by a factor of 2–3.

In type II-Plateau SNe, the continuum opacity dominates at early times throughout most of the optical, and even at late times, there are fairly clean “continuum” regions devoid of line opacity and emissivity, for example, between $H\alpha$ and the Ca II triplet at 8500 Å (Dessart & Hillier 2005). In type IIb/Ib/Ic, the large abundance of He (and its low ionisation in the photospheric layers) and intermediate mass elements reduces the importance of continuum opacity sources and favours the role of lines (Fig. 24). Electron scattering is sub-dominant and may represent only a third of the total Rosseland-mean opacity, even at bolometric maximum.

As time progresses and the ejecta turns nebular, the influence of lines grows. In our simulations, this causes the steep decline of the continuum flux below the representative flux level of the model, which only shows a quasi-continuum (Fig. 25). The emergent spectrum even at the peak is a collection of overlapping lines, causing simultaneous absorption, scattering, and emission. P-Cygni profile formation is altered from the general conception since it is not continuum photons that interact with the line but instead the background radiation arising from overlapping lines.

8 INFERENCE OF THE EJECTA EXPANSION RATE

One important characteristics of SN ejecta is their kinetic energy. It represents the left-over explosion energy after unbinding the progenitor envelope. To infer the ejecta kinetic energy, we need to infer its expansion rate. It is customary in the community to do this by constraining the location of the photosphere.

However, it is clear from the preceding section that photons subject to continuum opacity will decouple much deeper in the ejecta than photons overlapping with a strong line, such as $H\alpha$ in a SN IIb at early time. To different lines correspond a whole range of intermediate heights and legitimate but distinct photospheres.

Determining the location of these photospheres is nonetheless an interesting exercise. Using the location of maximum absorption, one can constrain the chemical stratification of an ejecta, bearing in mind that a line profile is also subject to multiple processes and uncertainties (e.g., ionisation, details of atomic physics, blending). In Fig. 26, we show a spectral sequence in the optical for model 3p65Ax1. Using synthetic spectra for individual species, we can unambiguously determine the location of maximum absorption in lines of sufficient strength and not overlapping with other lines of the same ion. We show the results (one red mark for each line and each epoch) for $H\alpha$, He I lines at 5875.7 Å, 6678.1 Å, 7065.2 Å, and 10830.2 Å, O I 7773.0 Å, and the Ca II triplet at 8569.0 Å. We omit the lines from Fe II or Ti II in the blue part of the optical since their contributions overlap — we see broad absorptions with internal dips which prevent the unambiguous identification of a specific line.

The guidance of the model helps for the velocity measurement on the weak optical He I lines at early times, or the vanishingly small line strength of $H\alpha$ at and beyond bolometric maximum. It helps also with ambiguous dips. The depression at 8000 Å in the spectrum at 60.6 d is not caused by Ca II absorption at high velocity

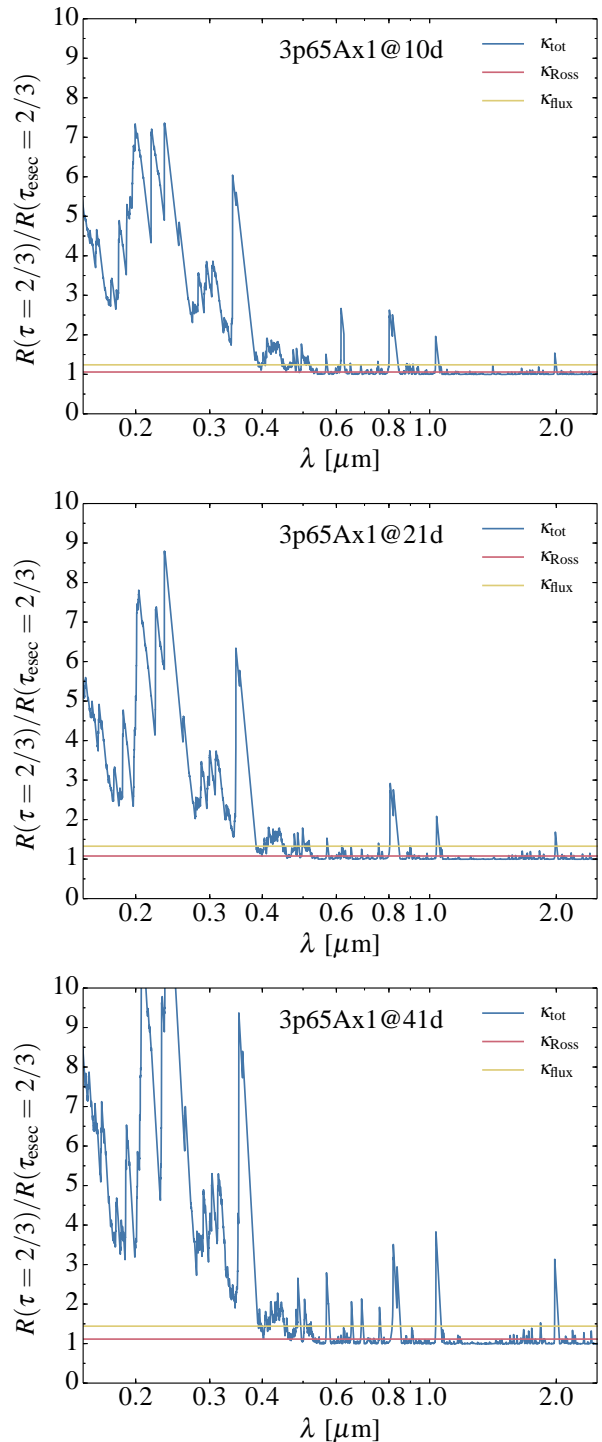


Figure 23. Wavelength variation of the photospheric radius $R(\tau = 2/3)$, normalised to the radius of the electron-scattering photosphere $R(\tau_{\text{esc}} = 2/3)$, when all opacity sources are included, and when we use the Rosseland-mean opacity κ_{Ross} or the flux-mean opacity κ_{flux} . From top to bottom, we show the results for model 3p65Ax1 at 10, 21, and 41 d after explosion. The distinct locations traced by each curve emphasise the ambiguity of the notion of a photosphere in these Type IIb/Ib/Ic SNe.

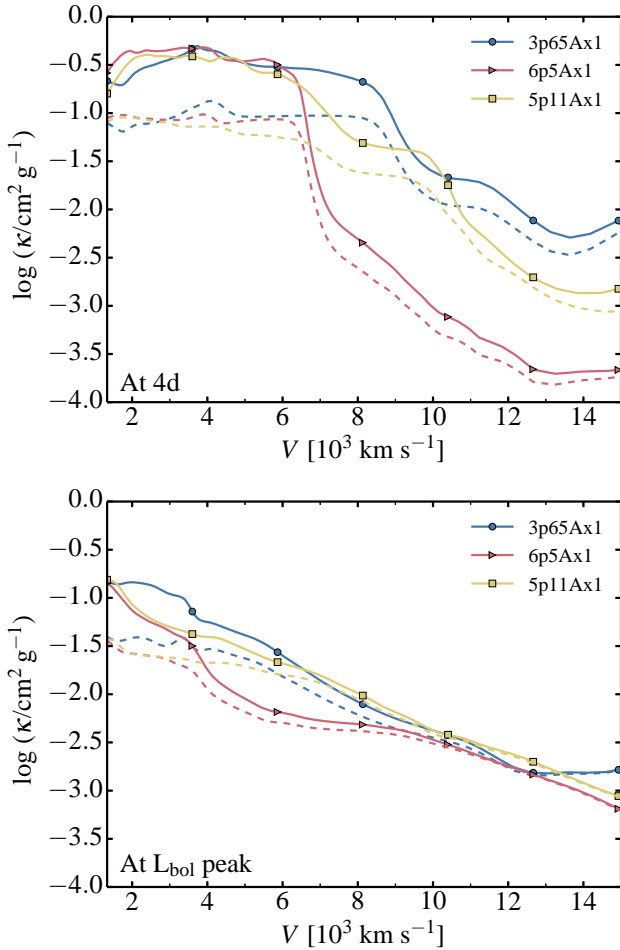


Figure 24. Variation of the mass absorption coefficient associated with the Rosseland-mean opacity κ_{Ross} (solid) and the electron-scattering opacity κ_{esec} (dashed) in the ejecta of models 3p65Ax1 (SN I Ib), 6p5Ax1 (SN Ib), and 5p11Ax1 (SN Ic) at ≈ 4 d after explosion (top) and at bolometric maximum (bottom). The same ordinate range is used in each panel. All opacities show a large variation with ejecta location, reflecting variations both in composition and ionisation (see also Fig 13). The range in mass absorption coefficient is significantly greater than for Type Ia SNe, which possess a more uniform composition (see, e.g., Fig. 12 in Dessart & Hillier 2015).

but corresponds to the blue edge of its emission. It also allows to establish with certainty that the progressive migration of the $1.05 \mu\text{m}$ absorption to larger velocity is associated with the broadening of the He I 10830 Å line, following the growth of the γ -ray mean free path and the non-thermal effects on He I in the outer ejecta.

Repeating the process for the other two models, we illustrate the trajectory of the velocity at maximum absorption for representative lines in Fig. 27 (we use the g -weighted mean wavelength for multiplets). In the type I Ib model, $v_{\text{abs}}(\text{H}\alpha)$ converges to $\approx 13000 \text{ km s}^{-1}$, which indeed corresponds to the base of the H-rich shell in the ejecta (Table 2). Some sudden variations can occur when line profiles have double dips of comparable strength or when the absorption is an extended trough. The jumps at early times may also arise when we switch on the treatment of non-thermal processes. However, overall, the evolution of all lines is to exhibit a maximum absorption that recedes in velocity space as we approach the time of bolometric maximum.

After maximum, non-local energy deposition and non-thermal processes alter the line opacity in the outer ejecta and lead to the broadening of the absorption troughs. The effect is strong in He I 10830 Å, whose maximum absorption occurs at 12000 km s^{-1} at late times. The chemical stratification matters here since He is systematically more abundant in the outer ejecta of these models — intermediate mass elements are less likely to exhibit this behaviour because their abundance peaks in the inner ejecta.

While the photosphere, and its associated velocity, are poorly defined, the representative ejecta velocity $v_m \equiv \sqrt{2E_{\text{kin}}/M_e}$ is a fundamental characteristic of the ejecta and an important parameter of analytical models for SN light curves. In our three simulations, we find that around bolometric maximum, this quantity is matched to within $\approx 10\%$ by $v_{\text{abs}}(\text{He I } 15875 \text{ Å})$ in model 3p65Ax1 ($v_m = 7476 \text{ km s}^{-1}$), or $v_{\text{abs}}(\text{O I } 7773 \text{ Å})$ in models 6p5Ax1 ($v_m = 5047 \text{ km s}^{-1}$) and 5p11Ax1 ($v_m = 5959 \text{ km s}^{-1}$). This correspondence is useful to constrain the ejecta kinetic energy and mass and drops the additional step, with its associated ambiguities, to locate “the” photosphere. In Paper II, we will study how the quantity v_m correlates with various lines in the full grid of models. This exploration also needs to be extended to progenitors with large surface radii.

9 CORRECTION FACTORS

Comparing a SN spectrum to a blackbody can give some information on the colour temperature. In type II SNe, the comparison is meaningful at early post-explosion times because there are extended continuum regions where the flux resembles a blackbody, merely “diluted” through the effect of scattering in the atmosphere (Mihalas 1978; Eastman et al. 1996; Dessart & Hillier 2005).

One must apply a correction to this blackbody spectrum in order to obtain the total luminosity and to infer the distance to a type II SN. Unfortunately, in practice, one is led not so much to correct for the effect of scattering but instead for the effect of lines (see discussion in Dessart & Hillier 2005). With type I Ib/Ic SNe, it is also possible to produce such correction factors, but the correction arises primarily from the effect of line emission/absorption. The second problem, as discussed above, is that there is no unambiguous photosphere, since it depends much on the opacity considered.

Nonetheless, we have repeated the calculations of Dessart & Hillier (2005) (this study was based on steady state models; correction factors for time-dependent simulations of type II SNe was discussed in Dessart & Hillier 2008) on the present set of models. We follow the procedure described in Section 2 of Dessart & Hillier (2005), and specifically compute the correction factors through a minimisation of their Equation 9. Since electron scattering is not a good representation of the total opacity, we employ the Rosseland mean instead and focus on times when the ejecta Rosseland-mean optical depth is $\gtrsim 10$ (i.e., the photospheric phase). Velocities associated with the photosphere, and how to infer them, can be gleaned from Fig. 27.

Correction factors show a complex behaviour (Fig. 28). Unlike type II SNe during the photospheric phase, which show a monotonic evolution towards cooler temperature at fixed photospheric composition (Dessart & Hillier 2011), type I Ib/Ic SNe exhibit a non-monotonic colour evolution (Fig. 4–6) with a photospheric composition that becomes progressively metal dominated. This is the reason for the bifurcation in the distribution of correction factors (compare the top row panels with the bottom row counterparts).

When we limit the time span to times around bolometric max-

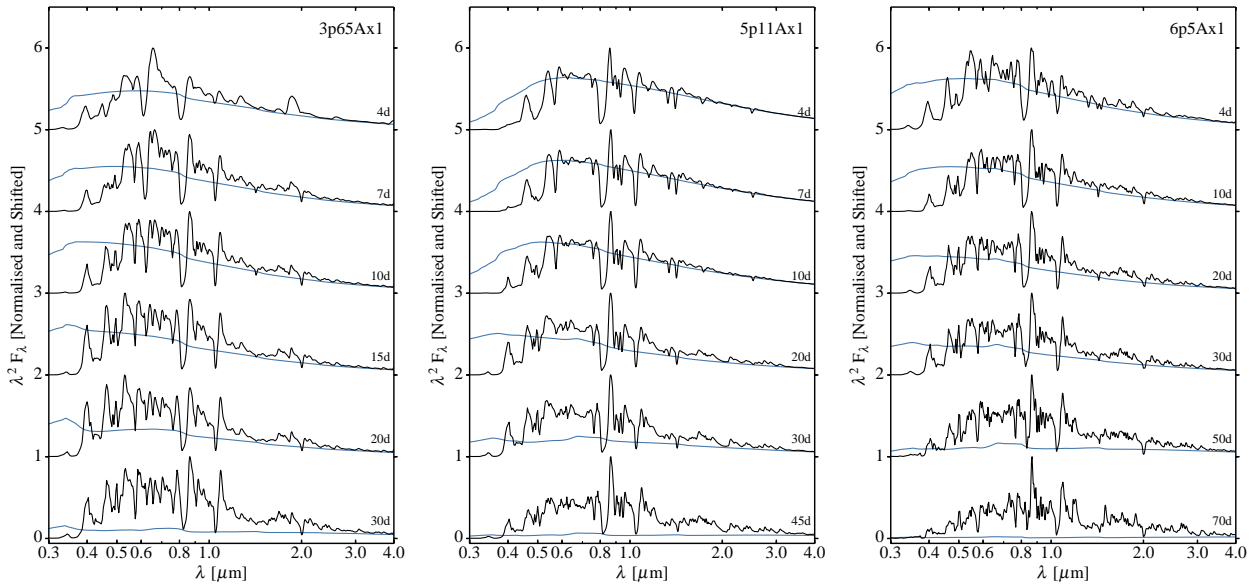


Figure 25. Evolution of the total flux (black) and the continuum flux (blue) in the optical and near-IR for the models 3p65Ax1, 5p11Ax1, and 6p5Ax1 during the photospheric phase. For better visibility of the near-IR, we show the quantity $\lambda^2 F_\lambda$. For the continuum flux calculation, only bound-free and free-free processes are included in the formal solution of the radiative-transfer equation. Note the growing separation between the total flux and the continuum flux as time progresses, caused by the increasing role played by lines over pure continuum processes. At many epochs no pure continuum region can be seen. In the optical, lines act through both emission and absorption, and in a very tangled way, while at early times in the UV lines cause a flux deficit through a blanketing effect.

imum, the distribution of points shows more uniformity (bottom row of Fig. 28). For convenience we have fitted the correction factors using a second-order polynomial in the inferred colour temperature. The polynomial coefficients are provided in Table 8. We also note that the correction factors are systematically offset between models, likely arising from the distinct composition in the atmospheres of each model.

These correction factors have to be used with circumspection. In Fig 29, we show the blackbody fits to the different optical bands for model 3p65Ax1 around bolometric maximum. The present context is far from the original notion of flux dilution in scattering atmospheres. The correction is instead used to recover from the questionable approximation of the model flux as a blackbody.

10 CONCLUSIONS

This paper is the first of a series describing a set of radiative transfer simulations for SNe Iib, Ib, and Ic from binary star progenitors. In this paper we focused our attention on three models that were selected for their distinct composition. Model 3p65A has a sizeable He-rich shell and some residual H in the outermost ejecta layers. It produces H I lines early on, and He I lines at all times, making it a Type Iib SN. Although more massive, the ejecta associated with model 6p5A is hydrogen deficient and has $1.65 M_\odot$ of He ($\approx 35\%$ by mass). It produces He I lines and is of Type Ib. Model 5p11A stems from a typical WC star composition, with a mixture of He, C, and O in the outermost ejecta. Even with strong mixing, it shows no He I line in the optical and is thus of Type Ic.

Despite these differences in composition, which produce different SN types, the qualitative properties of the bolometric light curves, multi-band light curves, and colours are comparable for all models. Having the same ejecta kinetic energy, the differences stem

primarily from the different ejecta masses. As expected, the higher the ejecta mass, the longer the rise time, the broader the light curve, and the slower the post-maximum decline rate. These properties stem from the greater trapping efficiency of low-energy photons (which in number make the bulk of the ejecta internal energy) and of high-energy photons (which originate from radioactive decay). About 80% of the total flux falls within the optical range, with the rest in the near-IR — little flux comes out in the UV except at very late times. At early times this holds because our progenitor models have small radii — it is not a fundamental property of all SNe Iib/Ib/Ic.

Quantitatively, Arnett’s rule does not produce a very accurate prediction of the ^{56}Ni mass — applied to our models it leads to an overestimate of the ^{56}Ni mass by about 50%. In contrast, the method of Katz et al. (2013) works very accurately with our models. Using an expression based on a solution of the energy equation, we can recover the original ^{56}Ni to within 5% by integrating the bolometric luminosity over time starting at 3 d after explosion (this offset can be reduced to $\lesssim 2\%$ if we take into account the trapped radiation energy at 3 d). The challenge with this method is the need to monitor the multi-band brightness from very early times (the later we start, the more inaccurate is the method), while a better accuracy requires the knowledge of the trapped radiation energy at the start of the integration.

As observed, we find that our models exhibit an earlier light-curve peak for bluer bands. Despite the uncertainties in mixing and ejecta mass/composition, the early post-maximum colours are comparable. The $(V - R)$ colour shows a good uniformity with a value of 0.32 mag (standard deviation of 0.04 mag). The effect of mixing is to enhance the brightness and make the SN bluer at early times. This leads to a flatter slope of the bolometric light curve as it ap-

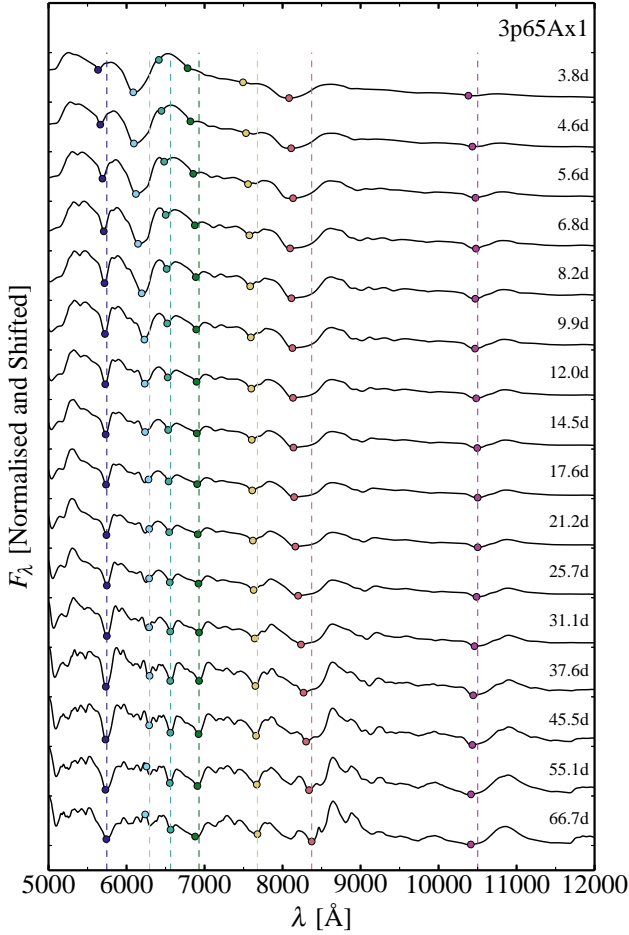


Figure 26. Spectral sequence for model 3p65Ax1 during the photospheric phase. We overlay the location at maximum absorption in H α , in the He I lines at 5875.7 Å, 6678.1 Å, 7065.2 Å, and 10830.2 Å, in O I 7773.0 Å, and in the Ca II triplet at 8569.0 Å. To better reveal the evolving velocity shifts for each transition, we also draw a vertical line (dashed and coloured) through the maximum absorption closest to the rest wavelength. With most features, the location of maximum absorption shifts to smaller velocities with time. However for He I 10830 Å this is only true initially – at late times the maximum absorption shifts to larger velocities due to the influence γ -rays and non-thermal effects in the outer ejecta.

proaches maximum. The effect of mixing on the multi-band light curves is only of minor importance after maximum.

We emphasise the spectral differences between our three models. We find that H α is eventually a good tracer of the velocity of the outer H-rich shell in a SN IIb. We also reproduce the non-monotonic behaviour of He I lines with time, which tend to become narrower from early time to bolometric maximum, before becoming broader again after maximum. This property is a vivid illustration of the combined effects of non-local (decay) energy deposition and non-thermal processes. This effect is primarily seen in He I lines, which are the most sensitive to non-thermal processes in these SNe.

While He is present in all our models, it can be difficult to identify in spectra. Due to blending, the 1.1 μ m region must be used with caution when trying to determine whether the ejecta contains He. In our type Ic model lines due to C I and Mg II are very important contributors to the P Cygni profile seen near 1.09 μ m,

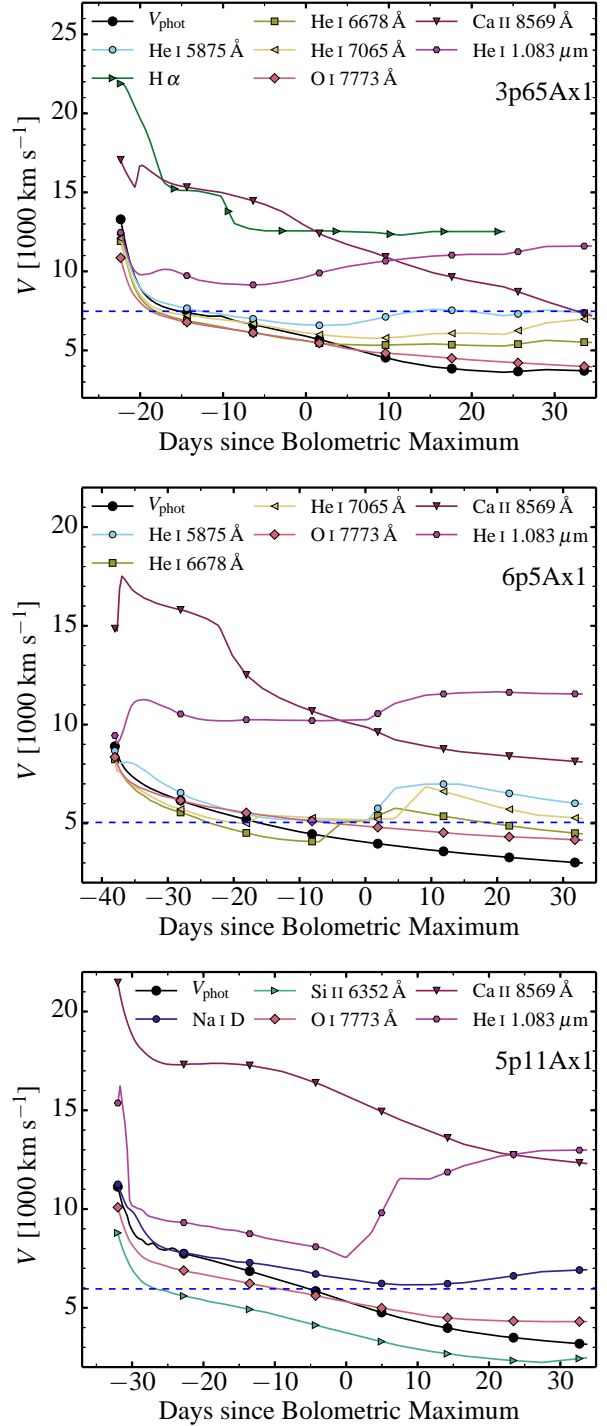


Figure 27. Evolution of the velocity at maximum absorption in representative lines for the three models 3p65Ax1 (SN IIb), 6p5Ax1 (SN Ib), and 5p11Ax1 (SN Ic). We use the gf -weighted mean wavelength for multiplets. We also add the photospheric velocity (for which we employ the Rosseland-mean opacity). The dashed line corresponds to the representative ejecta velocity given by $\sqrt{2E_{\text{kin}}/M_e}$.

while in the type IIb model Mg II is an important contributor. Other lines, such as He I 2.0581 μm , can be used to confirm the presence of He I in spectra, although the absence of this line does not preclude the presence of $\lambda 10830$.⁶ Paradoxically, in both our Ib and Ic models, He I 10830 Å is strongest at late times (≈ 70 d). Another method of distinguishing the type of progenitor is to use C I lines. We obtain weak or no C I lines in the 9000–11000 Å region prior to maximum in our SNe IIb/Ib models, which have a sizeable He-rich shell, while the SN Ic model, with its outer layers of He, C, and O, shows strong C I lines in this region.

Because a mass buffer rich in carbon and oxygen separates the helium-rich shell from the original site of ^{56}Ni , the production of He I lines in our models requires mixing. Without mixing, none of our models are of type Ib (or IIb), but would instead be of type Ic (or IIc) — see Dessart et al. (2012) for discussion. Furthermore, varying the mixing strength from moderate to strong (models x1 and x2) did not alter the SN type of these models. As done for observations, we discuss the SN type of each of our models based on its spectroscopic properties. However, it is clear from the characteristic width of their light curves that models 5p11A and 6p5A have a too low E_{kin}/M_e to match SN Ibc observations (see, for example, Drout et al. 2011).

As for SN Ia, a true continuum is only seen at very early times. After the spectrum formation zone recedes into the metal rich layers of the ejecta, metal line opacity and emissivity completely dwarf continuum processes. Line overlap then conspires to produce a quasi continuum. Consequently, the mass absorption coefficient is greater than that due to electron scattering, and varies with ionisation — it is not a constant in time or in depth. Furthermore, the ubiquity of lines in the spectrum formation region makes the notion of a well-defined photosphere obsolete.

Despite the complexities of spectrum formation, useful inferences about the ejecta can still be made. For example, the location of maximum absorption in various lines (e.g., H α or He I lines) can serve as a diagnostic of chemical stratification. We also discussed how the mean ejecta expansion rate, defined by $v_m = \sqrt{2E_{\text{kin}}/M_e}$ correlates with the P Cygni profile absorption velocity for various lines around the time of maximum. With a measure of both the mean expansion rate, and the ejecta mass, the energy of the SN explosion may be inferred.

Finally, we computed the correction factors to invoke when approximating the synthetic spectra with a blackbody. Because SN colours are affected by line opacity and emissivity, the correction depends on the selected band and on the adequacy of the model for a particular observation. We find that our models compare well to observations around the time of maximum (see Paper III) so the use of these correction factors should be limited to such epochs.

ACKNOWLEDGMENTS

LD acknowledges financial support from the European Community through an International Re-integration Grant, under grant number PIRG04-GA-2008-239184, and from “Agence Nationale de la Recherche” grant ANR-2011-Blanc-SIMI-5-6-007-01. DJH acknowledges support from STScI theory grant HST-AR-12640.01,

⁶ The lower levels of the $\lambda 10830$ transition ($1s\ 2s\ ^3S$) and of the $\lambda 20581$ transition ($1s\ 2s\ ^1S$) are metastable but the former has a longer lifetime (the $1s\ 2s\ ^1S$ level can decay by two-photon emission). Hence, the associated line optical depth can be significantly higher for the $\lambda 10830$ transition than for the $\lambda 20581$ transition.

and NASA theory grant NNX14AB41G. SW was supported by NASA (NNX14AH34G) and the DOE High Energy Physics Program (DE-SC-00010676). S.-C. Y was supported by the Basic Science Research (2013R1A1A2061842) program through the National Research Foundation of Korea (NRF). This work was granted access to the HPC resources of CINES under the allocation c2013046608 made by GENCI (Grand Equipement National de Calcul Intensif).

REFERENCES

- Arnett, W. D. 1982, *ApJ*, 253, 785
 Benvenuto, O. G., Bersten, M. C., & Nomoto, K. 2013, *ApJ*, 762, 74
 Bersten, M. C., Benvenuto, O. G., Nomoto, K., Ergon, M., Folatelli, G., Sollerman, J., Benetti, S., Botticella, M. T., Fraser, M., Kotak, R., Maeda, K., Ochner, P., & Tomasella, L. 2012, *ApJ*, 757, 31
 Blondin, S., Dessart, L., & Hillier, D. J. 2015, *MNRAS*, 448, 2766
 Blondin, S., Dessart, L., Hillier, D. J., & Khokhlov, A. M. 2013, *MNRAS*, 429, 2127
 Busche, J. R. & Hillier, D. J. 2005, *AJ*, 129, 454
 Claeys, J. S. W., de Mink, S. E., Pols, O. R., Eldridge, J. J., & Baes, M. 2011, *A&A*, 528, A131
 Dessart, L. & Hillier, D. J. 2005, *A&A*, 439, 671
 —. 2008, *MNRAS*, 383, 57
 —. 2011, *MNRAS*, 410, 1739
 —. 2015, *MNRAS*, 447, 1370
 Dessart, L., Hillier, D. J., Blondin, S., & Khokhlov, A. 2014, *MNRAS*, 441, 3249
 Dessart, L., Hillier, D. J., Li, C., & Woosley, S. 2012, *MNRAS*, 424, 2139
 Dessart, L., Hillier, D. J., Livne, E., Yoon, S.-C., Woosley, S., Waldman, R., & Langer, N. 2011, *MNRAS*, 414, 2985
 Dessart, L., Hillier, D. J., Waldman, R., & Livne, E. 2013a, *MNRAS*, 433, 1745
 Dessart, L., Livne, E., & Waldman, R. 2010a, *MNRAS*, 408, 827
 —. 2010b, *MNRAS*, 405, 2113
 Dessart, L., Waldman, R., Livne, E., Hillier, D. J., & Blondin, S. 2013b, *MNRAS*, 428, 3227
 Drout, M. R., Soderberg, A. M., Gal-Yam, A., Cenko, S. B., Fox, D. B., Leonard, D. C., Sand, D. J., Moon, D.-S., Arcavi, I., & Green, Y. 2011, *ApJ*, 741, 97
 Eastman, R. G., Schmidt, B. P., & Kirshner, R. 1996, *ApJ*, 466, 911
 Ensmann, L. M. & Woosley, S. E. 1988, *ApJ*, 333, 754
 Ergon, M., Sollerman, J., Fraser, M., Pastorello, A., Taubenberger, S., Elias-Rosa, N., Bersten, M., Jerkstrand, A., Benetti, S., Botticella, M. T., Fransson, C., Harutyunyan, A., Kotak, R., Smartt, S., Valenti, S., Bufano, F., Cappellaro, E., Fiaschi, M., Howell, A., Kankare, E., Magill, L., Mattila, S., Maund, J., Naves, R., Ochner, P., Ruiz, J., Smith, K., Tomasella, L., & Turatto, M. 2014, *A&A*, 562, A17
 Filippenko, A. V., Barth, A. J., Matheson, T., Armus, L., Brown, M., Espey, B. R., Fan, X.-M., Goodrich, R. W., Ho, L. C., Junkkarinen, V. T., Koo, D. C., Lehnert, M. D., Martel, A. R., Mazzarella, J. M., Miller, J. S., Smith, G. H., Tytler, D., & Wirth, G. D. 1995, *ApJL*, 450, L11+
 Fryxell, B., Arnett, D., & Müller, E. 1991, *ApJ*, 367, 619
 Hachinger, S., Mazzali, P. A., Taubenberger, S., Hillebrandt, W., Nomoto, K., & Sauer, D. N. 2012, *MNRAS*, 422, 70

Table 8. Coefficients of the second-order polynomial used to fit the distribution of correction factors for different optical-band combinations and for models 3p65Ax1, 5p11Ax1, and 6p5Ax1 over the time span $[t_{\max}/5, 1.1 \times t_{\max}]$. The polynomial is of the form $\xi(T) = \sum_{i=0}^2 a_i (1/T_4)^i$, where T_4 is the temperature in units of 10^4 K.

Coef.	3p65Ax1			5p11Ax1			6p5Ax1		
	(B, V)	(B, V, I)	(V, I)	(B, V)	(B, V, I)	(V, I)	(B, V)	(B, V, I)	(V, I)
a_0	1.5399	0.1629	0.2439	0.8836	-0.0089	-0.2657	-7.2109	1.3178	-0.9906
a_1	-2.2443	-0.1098	-0.1454	-0.9726	0.3429	0.9011	5.0819	-1.2462	2.1061
a_2	1.2820	0.4347	0.4417	0.6640	0.0924	-0.2389	-0.3316	0.6604	-0.6237

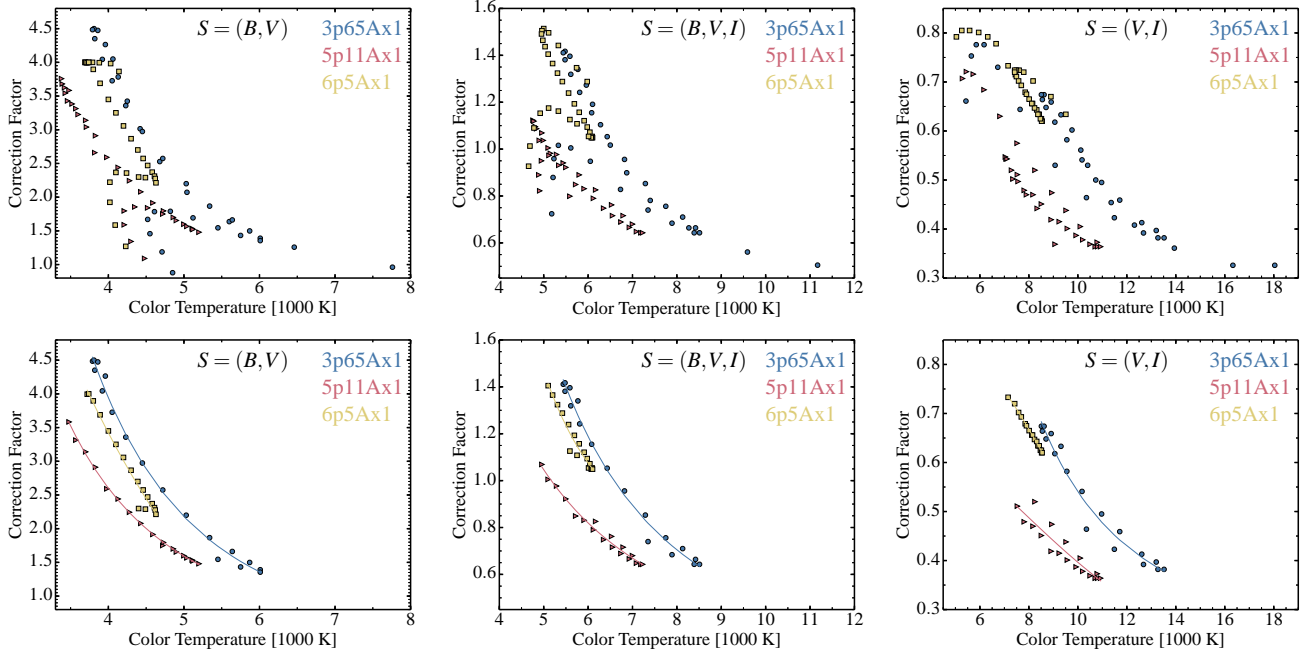


Figure 28. *Top row:* Distribution of correction factors for models 3p65Ax1, 5p11Ax1, and 6p5Ax1 for optical band combinations $S = (B, V)$ (left), (B, V, I) (middle), (V, I) (right), and based on photospheric-phase epochs. Each set S must contain at least two bands to constrain the colour temperature. *Bottom row:* Same as top, but now limiting the epochs to the range $[t_{\max}/5, 1.1 \times t_{\max}]$, where t_{\max} is the time of bolometric maximum. Also plotted is a fit to the distribution of correction factors using a second-order polynomial. The coefficients of the fitted polynomial are given in Table 8. The correction factors and color temperatures shown here are tabulated in the appendix.

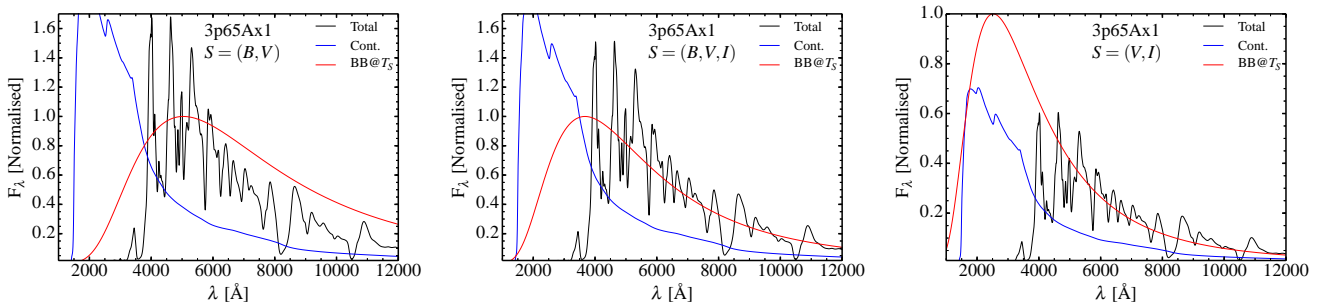


Figure 29. Comparison, near the time of bolometric maximum, of the total and continuum fluxes for model 3p65Ax1 with the blackbody flux computed with the associated correction factor and colour temperature T_S (see Table A1 in the appendix). From left to right, we show the results for the sets $S = (B, V)$, (B, V, I) , and (V, I) .

- Hammer, N. J., Janka, H.-T., & Müller, E. 2010, *ApJ*, 714, 1371
- Hillier, D. J. 1991, *A&A*, 247, 455
- Hillier, D. J. & Dessart, L. 2012, *MNRAS*, 424, 252
- Jerkstrand, A., Ergon, M., Smartt, S. J., Fransson, C., Sollerman, J., Taubenberger, S., Bersten, M., & Spyromilio, J. 2015, *A&A*, 573, A12
- Katz, B., Kushnir, D., & Dong, S. 2013, arXiv:1301.6766
- Kifonidis, K., Plewa, T., Scheck, L., Janka, H.-T., & Müller, E. 2006, *A&A*, 453, 661
- Li, C., Hillier, D. J., & Dessart, L. 2012, *MNRAS*, 426, 1671
- Livne, E. 1993, *ApJ*, 412, 634
- Lucy, L. B. 1991, *ApJ*, 383, 308
- Meikle, W. P. S., Cumming, R. J., Geballe, T. R., Lewis, J. R., Walton, N. A., Balcells, M., Cimatti, A., Croom, S. M., Dhillon, V. S., Economou, F., Jenkins, C. R., Knapen, J. H., Meadows, V. S., Morris, P. W., Perez-Fournon, I., Shanks, T., Smith, L. J., Tanvir, N. R., Veilleux, S., Vilchez, J., Wall, J. V., & Lucey, J. R. 1996, *MNRAS*, 281, 263
- Mihalas, D. 1978, *Stellar atmospheres*, 2nd edition, San Francisco, W. H. Freeman and Co.
- Millard, J., Branch, D., Baron, E., Hatano, K., Fisher, A., Filippenko, A. V., Kirshner, R. P., Challis, P. M., Fransson, C., Panagia, N., Phillips, M. M., Sonneborn, G., Suntzeff, N. B., Wagoner, R. V., & Wheeler, J. C. 1999, *ApJ*, 527, 746
- Nakar, E. & Piro, A. L. 2014, *ApJ*, 788, 193
- Nugis, T. & Lamers, H. J. G. L. M. 2000, *A&A*, 360, 227
- Piro, A. L. & Nakar, E. 2013, *ApJ*, 769, 67
- Podsiadlowski, P., Joss, P. C., & Hsu, J. J. L. 1992, *ApJ*, 391, 246
- Sauer, D. N., Mazzali, P. A., Deng, J., Valenti, S., Nomoto, K., & Filippenko, A. V. 2006, *MNRAS*, 369, 1939
- Weaver, T. A., Zimmerman, G. B., & Woosley, S. E. 1978, *ApJ*, 225, 1021
- Wellstein, S. & Langer, N. 1999, *A&A*, 350, 148
- Wongwathanarat, A., Mueller, E., & Janka, H.-T. 2015, *A&A*, 577, A48
- Woosley, S. E., Eastman, R. G., Weaver, T. A., & Pinto, P. A. 1994, *ApJ*, 429, 300
- Woosley, S. E., Langer, N., & Weaver, T. A. 1995, *ApJ*, 448, 315
- Yoon, S., Woosley, S. E., & Langer, N. 2010, *ApJ*, 725, 940
- Yoon, S.-C. 2015, *Publications of the Astron. Soc. of Australia*, 32, 15

APPENDIX A: CORRECTION FACTORS FOR THE THREE REFERENCE MODELS

In this section, we tabulate the correction factors for each of the three models during the photospheric phase. These SNe IIb/Ib/Ic models correspond to explosions of stars from relatively modest progenitor radii, and thus with intrinsic colours that are relatively red prior to peak.

In the future, we will study explosions of WR stars with a more extended radius at death. For these, we expect bluer colours prior to maximum, and consequently different correction factors.

Table A1. Corrections factors for the 3p65Ax1 model sequence covering the photospheric phase. See Section 9 for discussion, as well as Dessart & Hillier (2005) for a description of the tabulated quantities and a presentation of the method used to calculate them.

Age	T_{BV}	ξ_{BV}	T_{BVI}	ξ_{BVI}	T_{VI}	ξ_{VI}	T_{phot}	R_{phot}	V_{phot}
[day]	[K]		[K]		[K]		[K]	[cm]	[km s ⁻¹]
2.360	7760.0	0.961	11170.0	0.505	18040.0	0.326	7426.022	3.863(14)	18943.610
2.600	6460.0	1.258	9590.0	0.561	16330.0	0.326	6990.782	4.064(14)	18093.070
2.860	5600.0	1.637	8270.0	0.664	13940.0	0.361	6638.097	4.216(14)	17060.560
3.150	5040.0	2.072	7400.0	0.781	12310.0	0.408	6493.325	4.328(14)	15901.340
3.470	4680.0	2.528	6870.0	0.899	11360.0	0.454	6570.802	4.373(14)	14586.0
3.820	4420.0	3.015	6500.0	1.017	10730.0	0.500	6711.424	4.388(14)	13295.980
4.200	4250.0	3.424	6280.0	1.104	10400.0	0.530	6837.968	4.441(14)	12236.960
4.620	4130.0	3.783	6100.0	1.191	10120.0	0.561	6948.506	4.496(14)	11263.120
5.080	4060.0	4.049	5960.0	1.273	9760.0	0.602	7072.313	4.535(14)	10331.840
5.590	3960.0	4.264	5770.0	1.340	9310.0	0.633	7014.261	4.625(14)	9575.254
6.150	3860.0	4.474	5590.0	1.396	8910.0	0.659	6944.160	4.765(14)	8967.916
6.760	3810.0	4.500	5480.0	1.417	8620.0	0.674	6863.244	4.981(14)	8527.549
7.440	3790.0	4.485	5440.0	1.411	8510.0	0.674	6801.329	5.268(14)	8194.578
8.180	3820.0	4.351	5480.0	1.381	8550.0	0.664	6780.774	5.615(14)	7944.819
9.0	3920.0	4.044	5610.0	1.319	8700.0	0.648	6804.780	6.029(14)	7753.137
9.900	4050.0	3.727	5810.0	1.242	9060.0	0.618	6865.623	6.505(14)	7604.410
10.890	4230.0	3.358	6080.0	1.155	9550.0	0.582	6956.454	7.035(14)	7477.017
11.980	4450.0	2.974	6430.0	1.053	10170.0	0.541	7055.816	7.629(14)	7370.751
13.180	4720.0	2.574	6820.0	0.956	10970.0	0.495	7154.051	8.282(14)	7273.257
14.500	5030.0	2.200	7290.0	0.853	11710.0	0.459	7241.006	8.974(14)	7163.545
15.950	5340.0	1.867	7750.0	0.756	12610.0	0.413	7128.274	9.891(15)	7177.419
17.550	5640.0	1.662	8130.0	0.710	13200.0	0.397	7332.842	1.044(15)	6882.652
19.310	5870.0	1.499	8420.0	0.664	13520.0	0.382	7314.003	1.118(15)	6699.158
21.240	6010.0	1.391	8510.0	0.643	13270.0	0.382	7248.240	1.189(15)	6478.925
23.360	6010.0	1.355	8390.0	0.643	12680.0	0.392	7136.445	1.256(15)	6222.907
25.700	5750.0	1.432	7890.0	0.684	11490.0	0.423	6985.835	1.323(15)	5959.559
28.270	5450.0	1.545	7350.0	0.740	10350.0	0.464	6795.695	1.376(15)	5631.556
31.100	5120.0	1.693	6730.0	0.828	9070.0	0.530	6550.404	1.400(15)	5208.424

Table A2. Corrections factors for the 5p11Ax1 model sequence covering the photospheric phase. See Section 9 for discussion, as well as Dessart & Hillier (2005) for a description of the tabulated quantities and a presentation of the method used to calculate them.

Age	T_{BV}	ξ_{BV}	T_{BVI}	ξ_{BVI}	T_{VI}	ξ_{VI}	T_{phot}	R_{phot}	V_{phot}
[day]	[K]		[K]		[K]		[K]	[cm]	[km s ⁻¹]
3.27	3820.0	2.660	5590.0	0.799	9070.0	0.369	4895.1	3.593(14)	12717.7
3.60	3710.0	3.040	5340.0	0.931	8340.0	0.442	5322.9	3.462(14)	11129.6
3.96	3600.0	3.227	5150.0	0.982	7900.0	0.470	5245.4	3.628(14)	10603.8
4.36	3520.0	3.383	4990.0	1.037	7560.0	0.497	5267.4	3.786(14)	10050.8
4.80	3460.0	3.428	4900.0	1.037	7350.0	0.502	5085.7	4.072(14)	9817.7
5.28	3430.0	3.543	4810.0	1.096	7070.0	0.543	5226.7	4.177(14)	9155.7
5.81	3390.0	3.680	4760.0	1.123	7040.0	0.547	5218.4	4.411(14)	8786.7
6.39	3380.0	3.758	4780.0	1.119	7110.0	0.543	5221.0	4.703(14)	8517.7
7.03	3420.0	3.625	4840.0	1.087	7290.0	0.520	5122.0	5.135(14)	8453.9
7.73	3480.0	3.584	4960.0	1.069	7530.0	0.511	5262.9	5.453(14)	8164.8
8.50	3570.0	3.314	5100.0	1.005	7810.0	0.479	5111.8	6.092(14)	8295.6
9.35	3700.0	3.140	5290.0	0.977	8170.0	0.470	5340.3	6.448(14)	7981.9
10.29	3830.0	2.912	5500.0	0.922	8510.0	0.451	5390.7	7.034(14)	7911.9
11.32	3980.0	2.591	5720.0	0.849	8910.0	0.419	5281.0	7.866(14)	8042.9
12.45	4130.0	2.441	5910.0	0.831	9240.0	0.415	5503.4	8.357(14)	7769.5
13.70	4280.0	2.244	6120.0	0.790	9570.0	0.401	5565.2	9.084(14)	7674.5
15.07	4430.0	2.079	6350.0	0.748	9930.0	0.387	5622.4	9.826(14)	7546.9
16.58	4590.0	1.915	6550.0	0.716	10200.0	0.378	5685.1	1.062(15)	7414.2
18.24	4730.0	1.796	6740.0	0.689	10500.0	0.369	5756.9	1.142(15)	7247.7
20.06	4860.0	1.700	6930.0	0.666	10710.0	0.364	5827.7	1.224(15)	7062.5
22.07	5000.0	1.599	7090.0	0.648	10810.0	0.364	5893.5	1.308(15)	6859.3
24.28	5110.0	1.535	7190.0	0.643	10930.0	0.364	5971.6	1.388(15)	6614.2
26.71	5200.0	1.480	7230.0	0.643	10790.0	0.373	6018.1	1.467(15)	6358.7
29.38	5120.0	1.521	7000.0	0.680	10100.0	0.405	6010.5	1.541(15)	6072.5
32.32	5040.0	1.567	6790.0	0.716	9520.0	0.438	5996.6	1.600(15)	5729.8
35.55	4900.0	1.654	6530.0	0.762	8940.0	0.474	5962.6	1.637(15)	5330.4
39.10	4720.0	1.750	6170.0	0.826	8250.0	0.520	5853.2	1.662(15)	4918.9
43.01	4520.0	1.841	5800.0	0.890	7520.0	0.575	5695.2	1.676(15)	4510.5
47.31	4350.0	1.855	5440.0	0.941	6820.0	0.630	5539.1	1.696(15)	4148.1
52.04	4210.0	1.796	5120.0	0.973	6170.0	0.684	5386.5	1.720(15)	3826.0
57.24	4210.0	1.590	4950.0	0.950	5730.0	0.716	5282.2	1.759(15)	3556.5
62.96	4300.0	1.343	4890.0	0.890	5450.0	0.721	5233.8	1.819(15)	3344.1
69.26	4480.0	1.091	4910.0	0.822	5290.0	0.707	5212.4	1.887(15)	3153.6

Table A3. Corrections factors for the 6p5Ax1 model sequence covering the photospheric phase. See Section 9 for discussion, as well as Dessart & Hillier (2005) for a description of the tabulated quantities and a presentation of the method used to calculate them.

Age	T_{BV}	ξ_{BV}	T_{BVI}	ξ_{BVI}	T_{VI}	ξ_{VI}	T_{phot}	R_{phot}	V_{phot}
[day]	[K]		[K]		[K]		[K]	[cm]	[km s ⁻¹]
3.89	4140.0	3.865	5980.0	1.288	9510.0	0.634	7456.4	2.991(14)	8899.9
4.28	4030.0	3.982	5740.0	1.347	8900.0	0.670	7297.6	3.126(14)	8452.5
4.71	3880.0	3.995	5330.0	1.442	8170.0	0.702	6731.3	3.317(14)	8152.2
5.18	3790.0	4.000	5110.0	1.496	7790.0	0.720	6531.2	3.518(14)	7860.7
5.70	3740.0	4.000	5000.0	1.514	7600.0	0.724	6403.5	3.762(14)	7639.7
6.27	3710.0	3.995	4960.0	1.505	7490.0	0.724	6318.4	4.036(14)	7450.4
6.90	3690.0	4.000	4950.0	1.491	7420.0	0.724	6265.5	4.337(14)	7274.3
7.59	3690.0	4.000	4980.0	1.464	7450.0	0.715	6242.4	4.660(14)	7105.5
8.35	3700.0	4.000	5030.0	1.437	7490.0	0.711	6244.4	5.009(14)	6943.2
9.19	3720.0	3.995	5100.0	1.405	7580.0	0.702	6268.5	5.390(14)	6788.7
10.11	3740.0	4.000	5200.0	1.365	7690.0	0.693	6306.2	5.808(14)	6649.1
11.12	3800.0	3.896	5310.0	1.324	7850.0	0.679	6359.4	6.245(14)	6500.4
12.23	3890.0	3.689	5420.0	1.288	8010.0	0.665	6410.8	6.726(14)	6365.4
13.45	4000.0	3.450	5560.0	1.239	8150.0	0.656	6471.9	7.213(14)	6207.1
14.80	4100.0	3.251	5690.0	1.193	8320.0	0.643	6524.5	7.733(14)	6047.1
16.28	4200.0	3.057	5800.0	1.157	8420.0	0.634	6550.7	8.278(14)	5885.1
17.91	4300.0	2.867	5910.0	1.121	8510.0	0.625	6576.9	8.860(14)	5725.8
19.70	4390.0	2.700	5980.0	1.094	8540.0	0.620	6585.9	9.458(14)	5556.5
21.67	4460.0	2.574	6040.0	1.072	8520.0	0.620	6585.2	1.008(15)	5381.5
23.84	4520.0	2.470	6090.0	1.054	8470.0	0.625	6574.4	1.069(15)	5192.2
26.22	4580.0	2.371	6100.0	1.049	8370.0	0.634	6555.7	1.130(15)	4989.7
28.84	4610.0	2.312	6090.0	1.049	8230.0	0.647	6522.3	1.193(15)	4789.5
31.72	4620.0	2.276	6070.0	1.049	8120.0	0.656	6474.0	1.256(15)	4583.8
34.89	4630.0	2.213	6010.0	1.054	7900.0	0.675	6394.5	1.324(15)	4393.7
38.38	4490.0	2.290	5750.0	1.108	7420.0	0.720	6240.1	1.397(15)	4214.1
42.22	4400.0	2.299	5590.0	1.126	7150.0	0.733	6090.4	1.472(15)	4034.7
46.44	4240.0	2.358	5330.0	1.162	6660.0	0.778	5863.9	1.550(15)	3862.5
51.08	4100.0	2.367	5110.0	1.175	6320.0	0.792	5665.2	1.622(15)	3676.1
56.19	4020.0	2.222	4920.0	1.153	5950.0	0.801	5453.5	1.699(15)	3499.6
61.81	4020.0	1.924	4780.0	1.090	5580.0	0.805	5268.7	1.778(15)	3330.0
67.99	4090.0	1.586	4690.0	1.013	5260.0	0.805	5140.7	1.855(15)	3158.2
74.79	4230.0	1.270	4660.0	0.927	5040.0	0.792	5063.5	1.933(15)	2992.2